Geol. Mag. **156** (5), 2019, pp. 772–800 © Cambridge University Press 2018
doi:10.1017/S0016756818000201

Petrogenesis of the Harsin–Sahneh serpentinized peridotites along the Zagros suture zone, western Iran: new evidence for mantle metasomatism due to oceanic slab flux

FATEMEH NOURI*†, YOSHIHIRO ASAHARA‡, HOSSEIN AZIZI§ & MOTOHIRO TSUBOI¶

*Mining Department, Faculty of Engineering, University of Kurdistan, Sanandaj, Iran
‡Department of Earth and Environmental Sciences, Graduate School of Environmental Studies,
Nagoya University, Nagoya 464-8601, Japan
§Mining Department, Faculty of Engineering, University of Kurdistan, Sanandaj, Iran
¶Department of Applied Chemistry for Environment, School of Science and Technology,
Kwansei Gakuin University, Sanda 669-1337, Japan

(*Received* 12 March 2017; *accepted* 16 February 2018; *first published online* 12 April 2018)

Abstract – The Harsin–Sahneh serpentinized peridotites are widely exposed along the Zagros suture zone in the western region of Iran and are considered to represent remnants of Neo-Tethys oceanic lithosphere at the junction of the Arabian and Iran Plates. These rocks are characterized by low contents of SiO_2 (38.8–43.5 wt %), Al_2O_3 (0.1–3.8 wt %), CaO (0.2–8.2 wt %) and TiO_2 ($<$ 1 wt %) and high MgO contents (31.1–46.0 wt %). Their enrichments of large ion lithophile elements and light rare earth elements, with high $^{87}Sr/^{86}Sr_{(i)}$ values (0.7036–0.7109) and relatively high variations in their $\varepsilon Nd_{(t)}$ (–7.5 to +7.8) values, indicate that the Harsin–Sahneh peridotites were metasomatized by flux released from the oceanic subducting slab in an active margin. The chemical compositions and isotopic ratios of these rocks suggest that they were formed as residue of mid-oceanic ridge basalt in the lithosphere that was then subsequently re-melted and metasomatized in a supra-subduction zone system. The occurrence of both mid-oceanic ridge and supra-subduction zone-type peridotites suggests that the heterogeneity of the upper mantle may have occurred due to the different ratios of partial melting and melt–rock reaction processes in different tectonic settings within the Neo-Tethys realm. The Harsin–Sahneh peridotites provide a good explanation of multistage melt extraction as well as melt–rock and metasomatic reactions in the mantle sequence of the Zagros ophiolite complex.

Keywords: Zagros suture zone, Neo-Tethys, metasomatic mantle, peridotite, partial melting, lithosphere

1. Introduction

Ultramafic rocks are dispersed in suture zones and orogenic belts as the basal sections of ophiolite complexes. They provide important information about melting, melt extraction processes and melt–rock interactions in the upper mantle (Zhou *et al.* 2005; Dilek, Furnes & Shallo, 2007; Eyuboglu, Santosh & Chung, 2011). Thus, geochemical data from peridotites and their constituent minerals can be used to characterize the origin and tectonic setting of ophiolitic rocks (Melcher *et al.* 2002; Karipi, Tsikouras & Hatzipanagiotou, 2006; Choi, Shervais & Mukasa, 2008; Aldanmaz *et al.* 2009; Pagé, Bédard & Tremblay, 2009; Pearce & Robinson, 2010; Ulrich *et al.* 2010). Peridotites may show surprisingly diverse variations (Parkinson *et al.* 1992; Parkinson & Pearce, 1998; Pearce *et al.* 2000), as they can range from relatively fertile peridotites to depleted restites that form after the extraction of large volumes of melt fraction (>20 %) under hydrous conditions (Jean *et al.* 2010; Uysal *et al.* 2012).

The Iranian Plate is a tectonically active region within the Alpine–Himalayan orogenic belt that is squeezed between the Afro-Arabian Plate in the southwest and the Eurasian Plate in the north. It is divided into several structural zones (Fig. 1) (Stöcklin, 1968). Within the Iranian Plate, a main remnant of oceanic basement is from the Neo-Tethys Ocean. The Neo-Tethys Ocean opened from the Late Carboniferous to Permian (Berberian & King, 1981; Davoudzadeh & Schmidt, 1984; Ricou, 1994; Besse *et al.* 1998; Mohajjel, Fergusson & Sahandi, 2003), as Cimerian continental fragments rifted from the northern margin of Gondwana. Oceanic crust developed along this fracture, and the subduction of this oceanic crust began during the Late Triassic to Early Jurassic (Berberian & King, 1981; Davoudzadeh & Schmidt, 1984; Ricou, 1994; Besse *et al.* 1998; Mohajjel, Fergusson & Sahandi, 2003; Davoudian *et al.* 2016). The Zagros orogenic belt is related to the opening and closure of the Neo-Tethys, and is divided into three units (Fig. 1): (1) the Urmia–Dokhtar magmatic arc (Fig. 1)

---

†Author for correspondence: F.nourisandiani@gmail.com

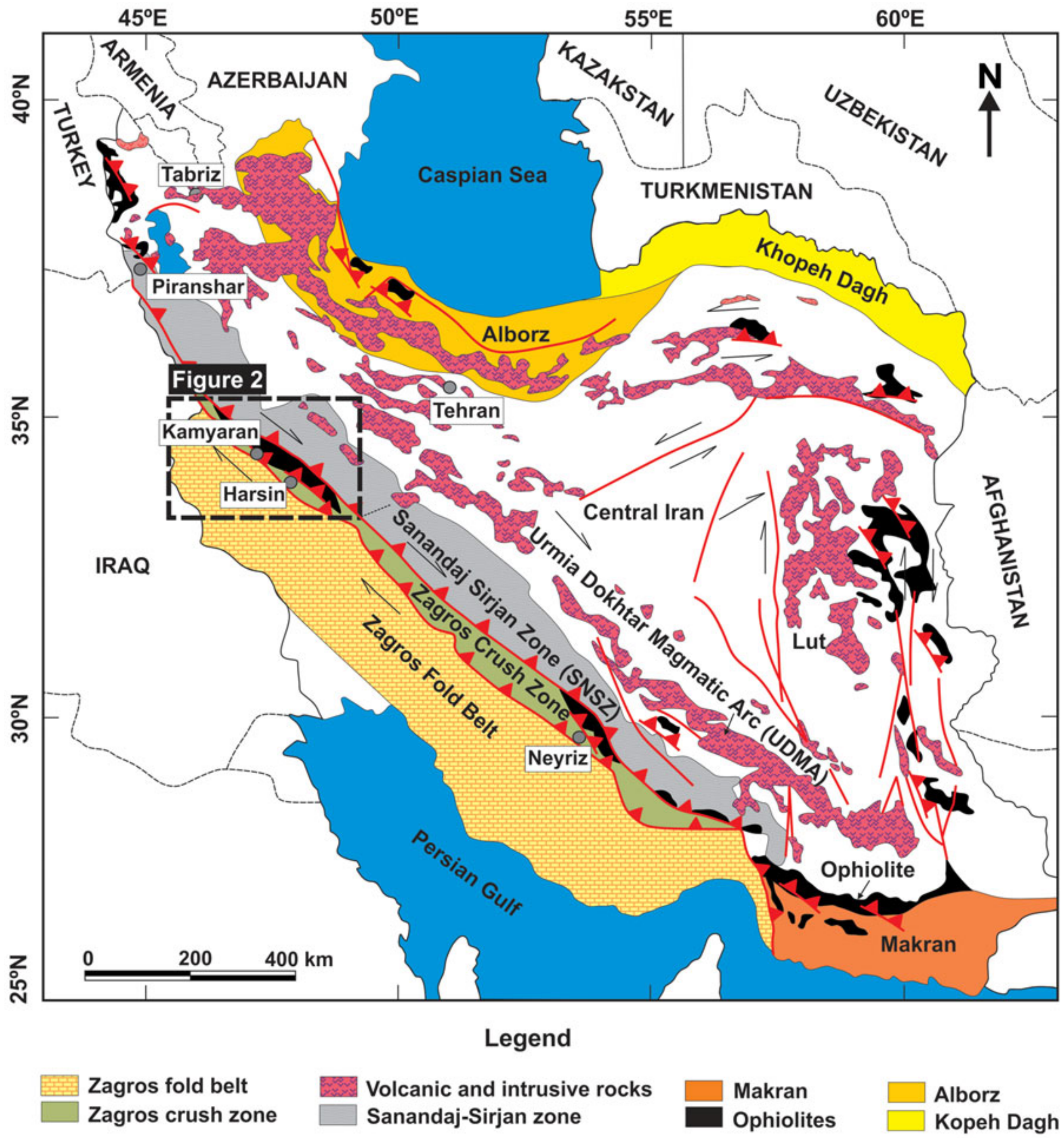

Figure 1. (Colour online) Simplified geological map of Iran (modified from Stöcklin, 1968).

was interpreted to be the product of the subduction of the Neo-Tethys oceanic slab beneath the central Iranian Plate. It records abundant Cenozoic magmatism, which is dominantly related to Eocene arc evolution (Berberian & King, 1981; Shahabpour, 2007; Omrani *et al.* 2008; Ghorbani & Bezanjani, 2011; Verdel *et al.* 2011; Ghorbani, Graham & Ghaderi, 2014). (2) The Sanandaj–Sirjan zone (SNSZ), which extends from SE to NW Iran (Fig. 1), was an active margin from the Middle Jurassic to Late Cenozoic and includes many granitoid intrusive bodies (Baharifar *et al.* 2004; Agard *et al.* 2005; Esmaeily *et al.* 2005; Davoudian *et al.* 2008; Aghazadeh *et al.* 2010; Azizi *et al.* 2011*a* , 2015*a*; Mahmoudi *et al.* 2011; Azizi, Zanjefili Beiranvand & Asahara, 2015*b*; Azizi, Kazemi & Asahara, 2017). (3) The Zagros fold-thrust belt, which consists of dismembered ophiolites and coloured mélanges, crops out along the Zagros suture zone at Neyriz and Esfandaghah in SW Iran and at Kermanshah and Piranshahr in W and NW Iran (Fig. 1). The ophiolites in the Zagros suture zone comprise relicts of Neo-Tethys oceanic lithosphere, which were finally emplaced during the closure of the ocean (Delaloye & Desmons, 1980; Desmons & Beccaluva, 1983; Ghazi & Hassanipak, 1999; Dilek & Ahmed, 2003; Alavi, 2004; Allahyari *et al.* 2010 Azizi *et al.* 2013; Saccani *et al.* 2013; Shafaii Moghadam & Stern, 2015; Nouri *et al.* 2016, 2017). The ophiolites in these belts are abundant and comprise various dismembered mafic–ultramafic assemblages that have suffered multiple phases of alteration and deformation. They display evidence of a variety of tectonic environments, ranging from a low degree of partial melting at a mid-oceanic ridge setting to a high degree of partial melting in an arc-related environment (Delaloye & Desmons, 1980; Ghazi & Hassanipak, 1999; Parlak, Höck

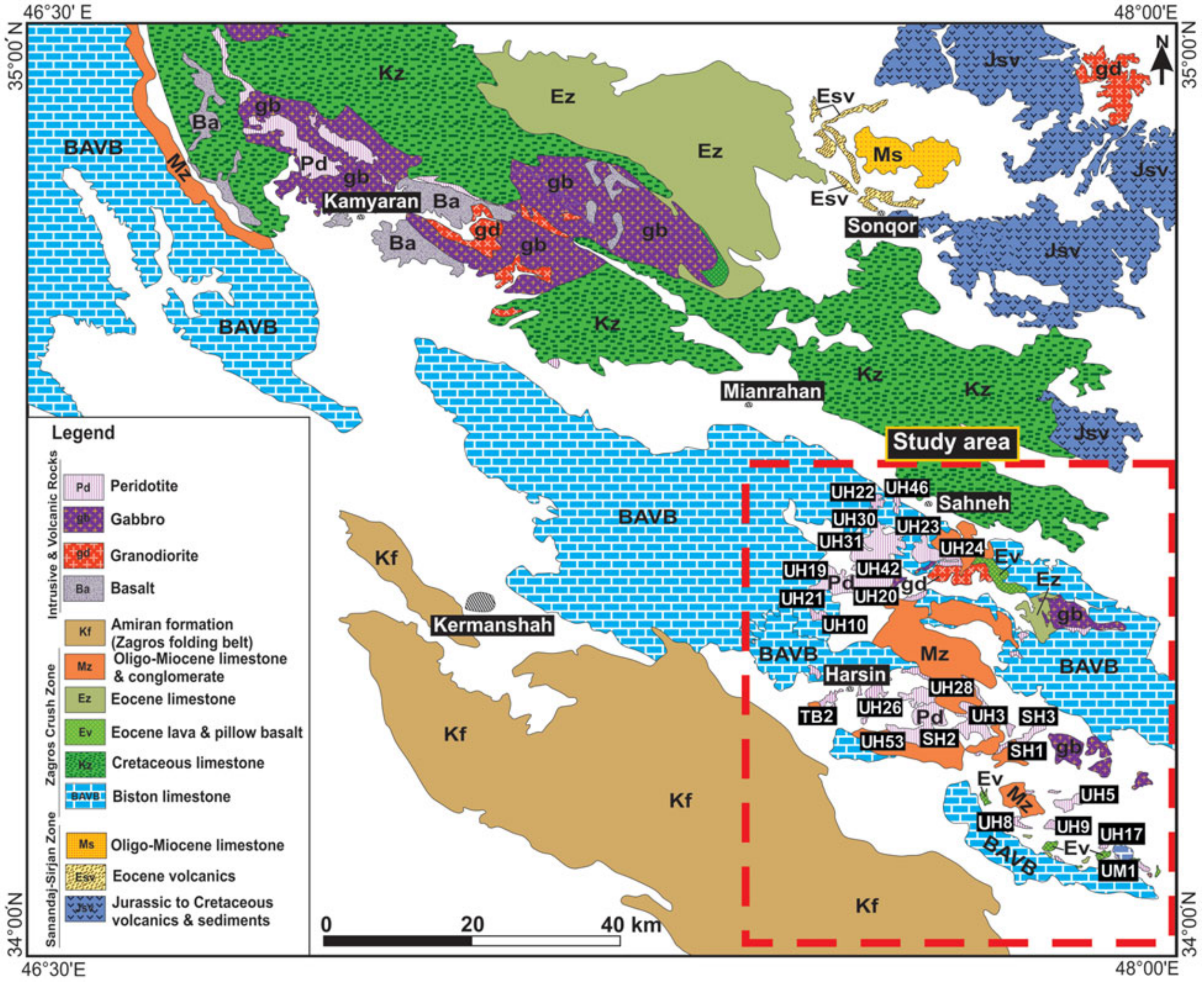

Figure 2. (Colour online) Simplified geological map of western Iran: Harsin area modified from Shahidi & Nazari (1997), Miyanrahan area from Rafia & Shahidi (2006), Kamyaran area from Sadeghian & Delvar (2006), Kermanshah area from Karimi Bavandpur & Hajihoseini (1999) and Sonqor area from Eshraghi, Jafarian & Eshraghi (1996). The surrounding broken line shows the Harsin area, and sampling locations are indicated.

& Delaloye, 2002; Dilek & Ahmed, 2003; Alavi, 2004; Allahyari *et al.* 2010, 2014; Uysal *et al.* 2012, 2016; Azizi *et al.* 2013; Saccani *et al.* 2013; Saka *et al.* 2014; Shafaii Moghadam & Stern, 2015; Ao *et al.* 2016; Nouri *et al.* 2016, 2017).

The Harsin–Sahneh ophiolite complex in eastern Kermanshah contains spectacular ophiolites and is located between the Arabian and Iranian Plates. It mainly includes ultramafic and gabbroic rocks, with minor felsic rocks (Fig. 2). Allahyari *et al.* (2010) demonstrated that the depleted peridotites in the Harsin–Sahneh area were generated during oceanic spreading that formed an oceanic arc basin. Some researchers (Delaloye & Desmons, 1980; Desmons & Beccaluva, 1983; Ghazi & Hassanipak, 1999; Saccani *et al.* 2013) have suggested that the Harsin–Sahneh ophiolite formed at a mid-ocean ridge or in island arc basins, whereas others (Wrobel Daveau *et al.* 2010; Azizi *et al.* 2013; Saccani *et al.* 2013; Nouri *et al.* 2016, 2017) have argued that this zone formed in an undeveloped oceanic basin that was affected by a mantle plume. In the current study, we present mineral chemistry data, whole-rock geochemical and isotopic data and geochronological data from serpentinized peridotites in the Harsin–Sahneh area along the Zagros suture zone in the eastern region of Kermanshah to identify the origin of the ultramafic rocks by comparing them with previously published data from other ultramafic rocks. The origin and tectonic affinity of the Harsin–Sahneh peridotites (HSP) are unclear because few studies (Shahidi & Nazari, 1997; Allahyari *et al.* 2010) have been performed on the HSP rocks and their original mineral assemblages have almost been eliminated due to the effects of serpentinization and tectonic activity. These new data are used to evaluate the formation processes (i.e. partial melting with subsequent metasomatism) and melt–rock interaction processes of the ophiolitic mantle peridotites in the Harsin–Sahneh area.

2. Regional geology and field relationships

The Harsin–Sahneh ophiolite complex is located between the cities of Harsin and Sahneh in eastern

Kermanshah, which is located in the western region of Iran (Fig. 2). This area mainly consists of Biston sedimentary rocks, Cretaceous ophiolitic rocks, Eocene gabbro and volcano-sedimentary rocks and Late Cretaceous granites (Braud, 1978; Delaloye & Desmons, 1980; Desmons & Beccaluva, 1983; Shahidi & Nazari, 1997; Ghazi & Hassanipak, 1999; Allahyari *et al.* 2010; Saccani *et al.* 2013; Whitechurch *et al.* 2013; Nouri *et al.* 2016, 2017).

The oldest rocks in this region are the Late Triassic to Cretaceous sedimentary rocks in the Biston area (Shahidi & Nazari, 1997). This body shows rough topography and is mainly massive, but it occasionally exhibits weak layering in some parts. It includes very thick crystalline limestone that crops out in most regions of the study area. The Cretaceous ophiolite complex comprises ultramafic, mafic and sedimentary mélange complexes that are divided by faults. It is difficult to clearly separate these rocks because they have been deformed and mixed with sediments. In most areas, dynamic deformation has affected the entire ophiolite complex; evidence of this deformation occurs as irregular blocks or bands within Eocene mafic and Miocene sedimentary rocks. The mafic rocks have been divided into two groups based on their intrusive age and tectonic setting: (1) Pillow basalt and coarse-grained gabbro that are black to white in colour represent Cretaceous ophiolites. Some researchers have suggested that these rocks have mid-ocean-ridge basalt (MORB) or/and within-plate origins (Allahyari *et al.* 2010; Allahyari, Pourmoafi & Khalatbari-Jafari, 2012). Ao *et al.* (2016) reported an age of 79.3 Ma for the rodingitic gabbros in this area. (2) The Eocene fine- to coarse-grained gabbros represent associated volcanic rocks. Braud (1978) suggested an Eocene age for some of the gabbroic bodies in the Harsin area. Whitechurch *et al.* (2013) and Ao *et al.* (2016), based on K–Ar and U–Pb age dating, reported ages of 56 Ma and 37 Ma for these gabbros in the northern Harsin area. These rocks are green to black in colour and exhibit rough morphology in outcrops. Our field observations show the gabbroic and sedimentary rocks were mélanged and in some areas the gabbroic and sedimentary rocks show pseudo-layer structures (Nouri, 2016). This group has been incorrectly mapped as layered gabbro on the Harsin map (Shahidi & Nazari, 1997). The trace element chemical compositions of these rocks, as well as their Sr and Nd isotopic ratios show they have affinities to an extensional tectonic regime due to the upwelling of metasomatized mantle after the Late Cretaceous collision in the Harsin area (Wrobel Daveau *et al.* 2010; Azizi *et al.* 2013; Saccani *et al.* 2013; Nouri *et al.* 2016, 2017). New field works by Wrobel Daveau *et al.* (2010) show the presence of detachment faults over mantle rocks that associate to upwelling of mantle. Furthermore, Braud (1978), Whitechurch *et al.* (2013) and Nouri *et al.* (2017) proposed that the body formed in an Eocene arc to back-arc setting.

The serpentinized peridotites are characterized by flat morphology; they form elevations or swelling hills that are supported by scarce vegetation (Fig. 3a). This massif chiefly includes serpentinized harzburgite and lherzolite with lenses of dunite that vary in size. Serpentinite bodies exhibit faulted and sheared contact relationships where they are exposed. Sometimes, relic lenses are schistose serpentinites and they are brecciated. Carbonate assemblages are locally developed close to the shear zone between the serpentinite and the ophiolite mélange. Farther from the shear zone, the protolith of serpentinite can be easily recognized as harzburgite, in which relicts of primary orthopyroxenes are still preserved in the serpentinized background. Serpentinized dunites are observed as tectonic slices within gabbro and limestone (Fig. 3b, c). The serpentinized peridotites are always sandwiched between Eocene and Miocene sediments and are bounded by faults (Fig. 3d, e). The cavities and fractures in the HSP rocks are filled by silica fluid that was derived from the late-stage injection of granitic magma during the Late Cretaceous (Nouri *et al.* 2016). The peridotites exhibit faulted relationships with the rodingitic gabbros (Fig. 3f). The rodingitic gabbros formed by a metasomatic mechanism that involved the loss of Si and alkalis from a mafic protolith during or after the serpentinization of adjacent ultramafic rocks (Nouri & Azizi, 2015) (Fig. 3g). Some peridotites exhibit faulted relationships with felsic rocks (Fig. 3h) and occur as isolated bodies and slices within the felsic bodies. They are locally cut by felsic rocks (Fig. 3i) of Late Cretaceous age (Nouri *et al.* 2016), thus indicating that the HSP bodies are older than the felsic dikes.

3. Petrography

The Harsin–Sahneh peridotites (HSP) are mostly serpentinized and display porphyroclastic to mesh textures. The porphyroclasitc to mesh textures indicate that the rocks are tectonites. They mainly comprise olivine, orthopyroxene, scarce clinopyroxene and spinel with varying amounts of serpentinized minerals. The deformed minerals display undulose extinction and kink-band fractures; these textural features are evidences of mantle metamorphism.

Olivine generally forms elongated porphyroclasts that have been partially replaced by serpentine and show a typical mesh texture (Fig. 4a). Olivine neoblasts occur around orthopyroxene grains (Fig. 4b); the olivine neoblasts are evidence of annealing. Orthopyroxene porphyroclasts exhibit strongly corroded boundaries with embayments that have been filled by olivine and spinel. They also exhibit clinopyroxene exsolution lamellae (Fig. 4c). Orthopyroxene is frequently replaced by bastite serpentine, which is dark brown to black in colour (Fig. 4b, d). Spinel inclusions are observed in some orthopyroxene and olivine porphyroclasts (Fig. 4d). In addition, there are minor primary clinopyroxene porphyroclasts with irregular rims, which represent the residues left after partial

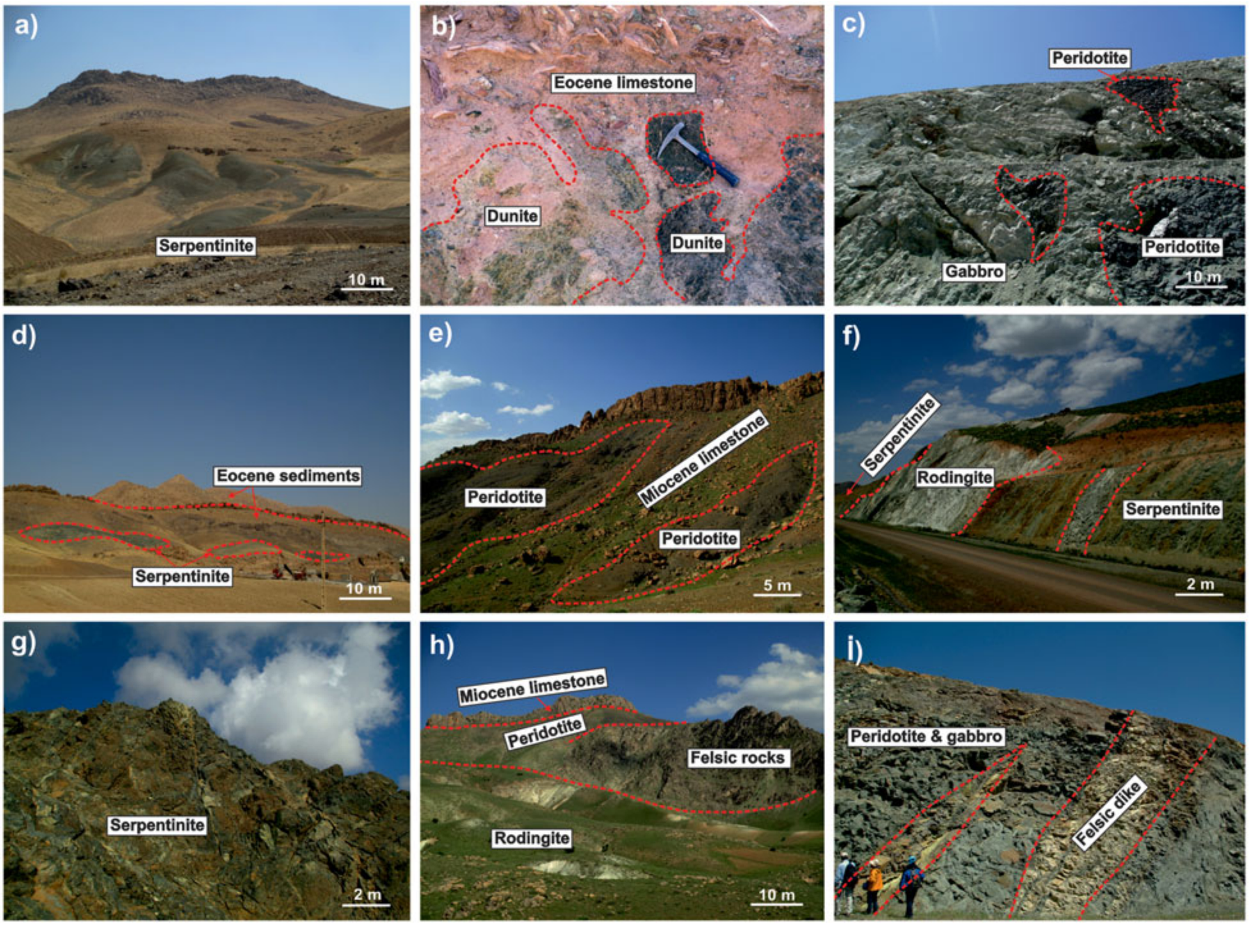

Figure 3. (Colour online) Photographs of HSP bodies from the Harsin area. (a) Serpentinized peridotites with smooth morphology. (b) Serpentinized dunites as tectonic slices within limestone. (c) Serpentinized dunites as tectonic slices within gabbro. (d) Irregular blocks of serpentinites within Eocene sedimentary rocks. (e) Irregular blocks or bands of peridotites within Miocene sedimentary rocks. (f) Fault relationship between serpentinized HSP rocks and rodingitic gabbro. (g) Hydrothermal alteration in the HSP rocks. (h) Fault relationship of the HSP rocks with felsic rocks, gabbro and Miocene sediments. (i) Felsic dikes in the HSP rocks.

melting (Fig. 4e, f) (Zhou *et al.* 2005; Uysal *et al.* 2012). Secondary clinopyroxene commonly occurs as an interstitial phase along the grain boundaries of olivine (Fig. 4a, g) and orthopyroxene. This indicates that the formation of clinopyroxene occurred during the last stage, and this type of clinopyroxene is interpreted to represent the product of the crystallization of metasomatic melts (Nicolas & Prinzhofer, 1983; Luguet *et al.* 2001; Alard *et al.* 2005; Morishita *et al.* 2007; Uysal *et al.* 2015). Amphibole tends to occur as irregular growths along the rims of clinopyroxene crystals. Accessory spinels exhibit anhedral to subhedral shapes; they are reddish-brown in colour and are randomly distributed in the serpentinized peridotite (Fig. 4h). They have been affected by deformation and show elongated grain shapes with incomplete ferrian chromite rims along their grain boundaries and fractures. In some samples, the spinel–orthopyroxene association shows a symplectic texture (Fig. 4h, i).

The relatively high abundances of relict olivine (~50–60 %) and orthopyroxene (~20–35 %) compared to the low abundances of pseudomorphic clinopyroxene relicts (~3–5 %) probably suggest that most of the HSP rocks originated from Cpx-harzburgites to harzburgites, as well as rare lherzolites and dunites.

4. Analytical techniques

Representative samples from the serpentinized HSP rocks were selected for chemical analyses based on their locations. The powdered samples were prepared and analysed for their major and trace element compositions. The whole-rock major element contents were determined using the wavelength dispersive X-ray fluorescence (WD-XRF) technique with a Rigaku ZSX Primus II at Nagoya University. For major element analyses, 0.5 g of each rock powder sample was mixed with 5.0 g of lithium tetraborate, and the mixture was melted at 1200 °C for 12–17 min with a high-frequency bead sampler to obtain a glass bead for XRF analysis. The whole-rock Cr and Ni contents were also determined using WD-XRF, and a glass bead was prepared for trace element analysis from a mixture of 1.5 g of sample powder and 5.0 g of lithium tetraborate. The loss on ignition (LOI) of the sample was calculated based on the weight difference after ignition at 950 °C.

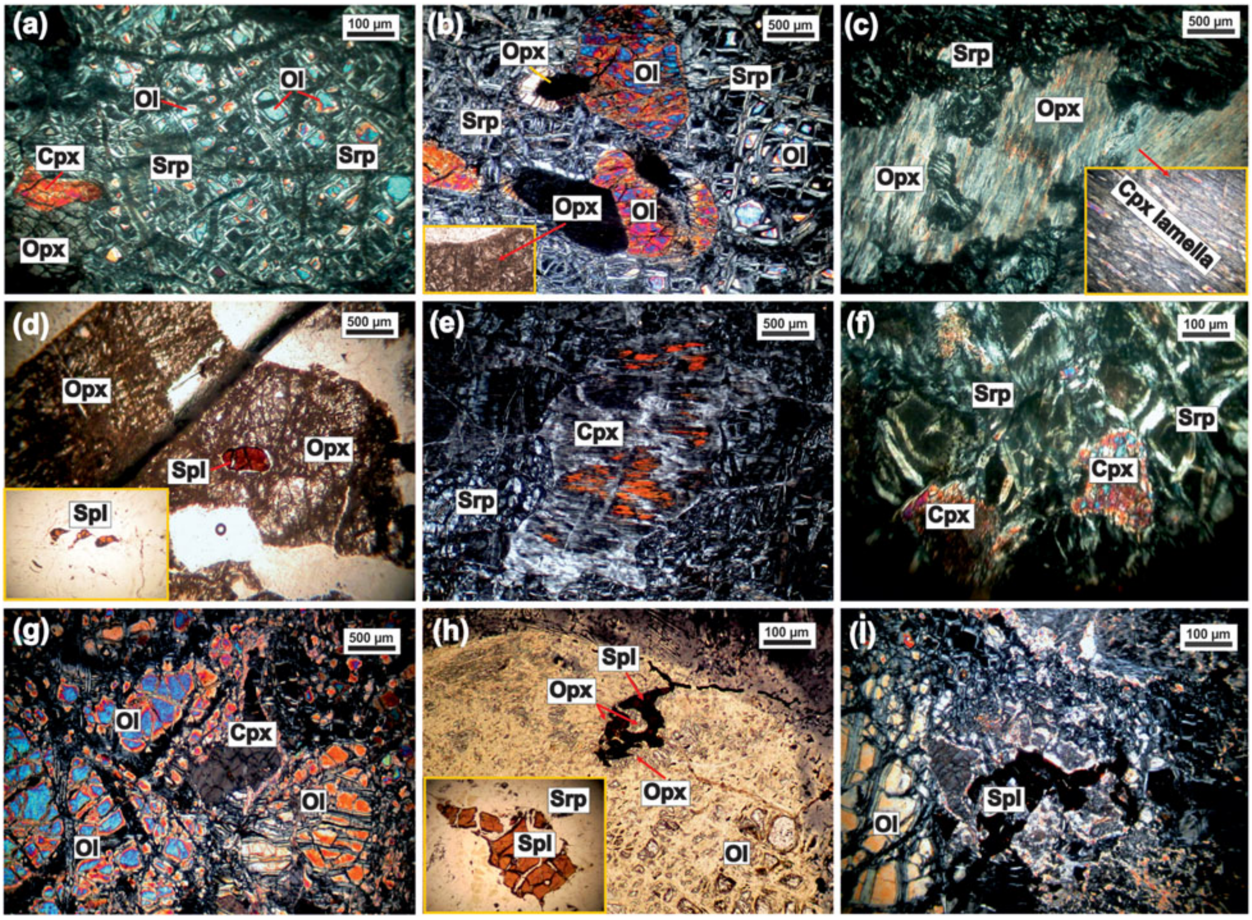

Figure 4. (Colour online) Thin-section images of the HSP rocks from the ophiolite. (a) Peridotite showing mesh texture and remnants of olivines (XPL). (b) Peridotite showing porphyroblastic textures. Olivine neoblasts occur around orthopyroxene grains (XPL). (c) Orthopyroxene porphyroclasts showing clinopyroxene exsolution lamellae (XPL). (d) Spinel inclusions observed in some orthopyroxene porphyroclasts (PPL). (e, f) Clinopyroxene porphyroblasts with irregular rims (XPL). (g) Secondary clinopyroxene occurring as an interstitial phase along grain boundaries with olivine. (h, i) Accessory spinels exhibiting anhedral to subhedral shapes with reddish-brown colour. Spinel–orthopyroxene association with a symplectic texture is observed (PPL). Ol: olivine; Srp: serpentine; Opx: orthopyroxene; Spl: spinel; Cpx: clinopyroxene (Whitney & Evans, 2010).

The HSP rocks contain low concentrations of rare earth elements (REE). Thus, 400–500 mg of each powdered sample was completely decomposed in 3 ml of HF (38 %) and 0.5–1 ml of $HClO_4$ (70 %) in a covered PTFE beaker at 120–140 °C on a hotplate in a clean room. The dissolved sample was then dried at 140 °C on a hotplate using infrared lamps. After drying, $>$10 ml of 2–6 M HCl was added to the dried sample to dissolve it, and the sample solution was moved to a polypropylene centrifuge tube to separate the residue from the clear upper portion. The residue was moved into a smaller PTFE vessel and then treated with $HF + HClO_4$ in a steel-jacketed bomb to ensure its complete dissolution. After the second HF decomposition, the residue fraction was mixed with the clear upper fraction, and the resulting solution was divided into two parts in a ratio of 1:20. The former was used for the quantitative analysis of trace elements, and the latter was used for Sr and Nd isotopic analysis. The former was dried and dissolved in 15–20 ml of 2 % HNO_3, and its concentrations of trace elements (including REEs) were analysed using an inductively coupled plasma mass spectrometer (ICP-MS) (Agilent 7700x) at Nagoya University. The latter was dried and dissolved in 15 ml of 2.4 M HCl. To isolate and purify Sr and REE, including Nd, from the large amount of matrix elements in $>$400 mg of rock sample, cation exchange column separation was carried out twice. First, after loading the sample solution (15 ml), matrix elements such as Fe, Mg and Ca were eliminated by a cation exchange column (AG50W-X8, 200–400 mesh) with an eluent of 2.4 M HCl, and both Sr and REE were collected together using an eluent of 6 M HCl. The collected Sr and REE fraction was dried and dissolved in 3 ml of 2.4 M HCl. The Sr and REE solution was loaded onto the same cation exchange column with eluents of 2.4 and 6 M HCl to isolate and collect Sr and REE, respectively, in each vessel. The REE fraction was dried, then neodymium was isolated from the REE fraction using a cation exchange column with an eluent of α-hydroxyl isobutric acid (α-HIBA).

The isotopic ratios of Sr and Nd were determined using the VG Sector 54-30 and GVI IsoProbe-T thermal ionization mass spectrometers (TIMS) at Nagoya University. Mass fractionation was corrected using values of $^{86}Sr/^{88}Sr = 0.1194$ and $^{146}Nd/^{144}Nd = 0.7219$. The NIST-SRM987 and JNdi-1 standards (Tanaka *et al.* 2000) were used as the natural Sr and Nd isotopic ratio standards.

For some of the samples, their elemental concentrations were determined using the isotope dilution (ID) technique after adding the prepared isotope spike solutions for Rb, Sr, Sm and Nd. To isolate Rb, Sr and REE, conventional column chemistry was carried out using cation exchange resin (Bio Rad AG50W-X8, 200–400 mesh) and an eluent of HCl. The abundances of Rb, Sr, Sm and Nd were measured using the Finnigan MAT Thermoquad THQ thermal ionization quadrupole mass spectrometer at Nagoya University.

Additionally, the trace element concentrations (including REE) of five samples (SH1, SH2, SH3, TB2, TM1) were analysed using inductively coupled plasma mass spectrometry (ICP-MS) at ALS CHEM Analytical Laboratories, North Vancouver, Canada.

After observations of the polished thin-sections were obtained, the chemical compositions of fresh minerals were determined using a JXA-8800R electron microprobe analyzer (EMPA) at Nagoya University. The acceleration voltage and beam current were set at 15 kV and 12 nA, respectively. Natural and synthetic standards were used for calibration.

5. Mineral chemistry

5.a. Spinel

Spinel grains are usually fresh and preserve their primary composition. The results of the electron microprobe (EMP) analyses of spinel in the HSP rocks are presented in Table 1a. Individually, there is no compositional variation or zoning in the spinels of the HSP rocks. These spinels are characterized by a narrow range of Cr_2O_3 contents of 35.3–42.3 wt% and Al_2O_3 contents ranging from 26.7 to 31.9 wt%. The Cr# varies from 0.44 to 0.52. The TiO_2 contents of spinels are low (<0.1 wt%), which is a common feature of ophiolitic ultramafic rocks (Arai & Yurimoto, 1994; Ahmed & Habtoor, 2015).

The minerals plot in the field of depleted peridotite (Fig. 5a) on the TiO_2 versus Cr# diagram (Dick & Bullen, 1984). The magnesium number (Mg#) values of the spinels in the HSP rocks (47.4–62.1) are generally higher than those in abyssal peridotites and SW Puerto Rico peridotites (i.e., mid-oceanic ridge rocks), and the Cr# values of the spinels are lower than those of boninites (Fig. 5b). The spinels of the HSP rocks plot close to the back-arc and eastern Cuba peridotite (i.e. back-arc basin) fields (Fig. 5b). Low Cr# (<0.6) values are typical indicators of oceanic ophiolites, including back-arc basin ophiolites, whereas arc-related ophiolitic spinels have Cr# values that are greater than 0.6 (Dick & Bullen, 1984).

5.b. Pyroxene

The results of the chemical compositions of the pyroxenes from the HSP rocks are listed in Table 1b. All analysed pyroxenes are chemically homogeneous.

The orthopyroxenes in the HSP rocks mainly comprise enstatite ($En_{80–90}$, $Wo_{1–14}$ and $Fs_{6–9}$), according to the pyroxene classification diagram (Fig. 5c) (Morimoto, 1988). Their Mg# values range from 91.3 to 95.3. These orthopyroxenes are characterized by narrow ranges of Al_2O_3 (2.5–3.6 wt%) and CaO contents (0.6–3.5 wt%), with low TiO_2 contents (<0.1 wt%). The orthopyroxenes show lower Al_2O_3 contents and higher Mg# values than MORB-type peridotites from SW Puerto Rico, and have similar compositions to back-arc peridotites from eastern Cuba (Fig. 5d).

The chemical compositions of representative clinopyroxene grains are also given in Table 1b. The residual clinopyroxenes are generally diopside in composition on the En–Wo–Fs ternary diagram (Morimoto, 1988). The Mg# values of clinopyroxene are positively correlated with their degree of depletion and degree of melting (Zhou *et al.* 2005; Uysal *et al.* 2012); clinopyroxenes in highly depleted peridotites are characterized by high Mg# values. The Mg# values of residual clinopyroxenes range from 90.7 to 92.1 (reflecting high degrees of partial melting) and are higher than those of the secondary clinopyroxenes with diopside compositions (Fig. 5c) that occur as an interstitial phase (i.e. Mg# values ranging from 84.1 to 86.6, reflecting melt–rock interactions). On the Al_2O_3 versus TiO_2 diagram (Fig. 5e), the clinopyroxenes plot in the field corresponding to a back-arc tectonic setting.

5.c. Olivine

The chemical compositions of olivines are shown in Table 1c. Both porphyroclastic and neoblastic grains show similar and homogeneous chemical compositions. The olivines in these samples plot in both the chrysolite and forsterite fields (Fig. 5f) on the olivine classification diagram (Deer, Howie & Zussman, 1992). The average Fo value in olivine reflects the fertility of a sample, and is related to the conditions of partial melting (i.e. the pressure and degree of melt extraction) (Arai, 1994; Uysal *et al.* 2012). The olivine porphyroclastic grains in the HSP rocks have variable Fo numbers ranging from 91.1 to 94.9 (reflecting a high degree of partial melting), whereas the neoblastic grains have variable Fo numbers ranging from 89.2 to 90.3 (due to melt–rock interactions). All of the olivines in the HSP rocks contain very low Ti and Cr concentrations, which are typically less than 0.1 wt%.

6. Whole-rock geochemistry

The whole-rock major and trace element compositions of the serpentinized HSP rocks are listed in Table 2. Their variable amounts of LOI values (1.0–6.8 wt%)

Table 1. Chemical compositions of (a) spinel, (b) pyroxene and (c) olivine, based on EMP analyses

(a)

Location	Sahneh								Harsin											
Sample	UH-21								UH-9						UH-8					
Mineral No.	Sp 1	Sp 2	Sp 3	Sp 4	Sp 5	Sp 6	Sp 7	Sp 8	Sp 9	Sp 10	Sp 11	Sp 12	Sp 13	Sp 14	Sp 15	Sp 16	Sp 17	Sp 18	Sp 19	Sp 20
SiO_2	0.018	0.018	0.015	0.016	0.016	0.021	0.020	0.042	0.061	0.050	0.026	0.049	0.025	0.025	0.022	0.011	0.039	0.038	0.019	0.037
TiO_2	0.019	0.030	0.046	0.009	0.000	0.016	0.016	0.013	0.038	0.045	0.084	0.000	0.000	0.020	0.015	0.025	0.044	0.034	0.020	0.023
Al_2O_3	29.04	28.89	28.36	27.41	29.23	29.23	26.73	29.11	28.55	27.40	28.27	29.28	28.71	28.28	31.86	27.43	27.32	27.05	26.68	27.27
Cr_2O_3	36.35	36.88	36.81	37.36	35.34	35.44	38.32	39.40	39.60	40.91	40.99	39.81	40.16	40.57	36.85	41.69	41.54	41.59	42.31	41.85
FeO	20.40	20.38	20.82	21.86	21.42	21.46	22.37	16.29	16.18	16.65	16.03	16.05	15.95	16.23	15.64	16.05	16.09	15.86	16.51	16.47
MgO	12.55	12.89	12.55	11.38	12.12	12.08	11.29	14.00	14.02	13.71	14.26	13.84	13.88	13.99	14.40	13.47	13.63	13.46	13.17	13.51
CaO	0.021	0.000	0.000	0.000	0.016	0.000	0.064	0.016	0.002	0.016	0.020	0.001	0.000	0.000	0.006	0.010	0.005	0.016	0.007	0.020
Na_2O	0.017	0.000	0.000	0.000	0.016	0.000	0.000	0.000	0.006	0.010	0.000	0.000	0.000	0.000	0.012	0.014	0.000	0.005	0.000	0.001
K_2O	0.003	0.000	0.008	0.000	0.000	0.007	0.000	0.002	0.007	0.021	0.004	0.002	0.003	0.019	0.000	0.007	0.000	0.000	0.011	0.000
(OH)	1.452	0.788	1.274	1.860	1.720	1.691	1.076	1.036	1.425	1.140	0.197	0.857	1.211	0.723	1.110	1.225	1.304	1.809	1.187	0.686
Total	100.00	100.00	100.00	100.00	100.00	100.00	100.00	100.00	100.00	100.00	100.00	100.00	100.00	100.00	100.00	100.00	100.00	100.00	100.00	100.00
Cation																				
Si	0.001	0.001	0.000	0.000	0.000	0.001	0.001	0.001	0.002	0.002	0.001	0.001	0.001	0.001	0.001	0.000	0.001	0.001	0.001	0.001
Ti	0.000	0.001	0.001	0.000	0.000	0.000	0.000	0.000	0.001	0.001	0.002	0.000	0.000	0.000	0.000	0.001	0.001	0.001	0.000	0.001
Al	1.040	1.027	1.016	0.998	1.051	1.050	0.971	1.029	1.015	0.978	0.995	1.034	1.019	1.001	1.112	0.981	0.977	0.974	0.959	0.972
Cr	0.873	0.879	0.885	0.912	0.852	0.854	0.933	0.935	0.944	0.979	0.968	0.944	0.956	0.963	0.863	1.001	0.996	1.005	1.020	1.001
Fe^{3+}	0.085	0.092	0.096	0.088	0.097	0.095	0.094	0.033	0.036	0.038	0.032	0.019	0.024	0.033	0.022	0.016	0.022	0.017	0.019	0.024
Fe^{2+}	0.433	0.422	0.433	0.477	0.450	0.452	0.482	0.376	0.372	0.384	0.368	0.383	0.378	0.375	0.365	0.391	0.386	0.389	0.402	0.393
Mg	0.568	0.579	0.569	0.524	0.551	0.549	0.519	0.626	0.630	0.619	0.635	0.618	0.623	0.626	0.636	0.610	0.616	0.613	0.599	0.609
Total	3.000	3.000	3.000	3.000	3.000	3.000	3.000	3.000	3.000	3.000	3.000	3.000	3.000	3.000	3.000	3.000	3.000	3.000	3.000	3.000
Mg#	52.3	53.0	51.8	48.1	50.2	50.1	47.4	60.5	60.7	59.5	61.3	60.6	60.8	60.6	62.1	59.9	60.1	60.2	58.7	59.4
Cr#	0.46	0.46	0.47	0.48	0.45	0.45	0.49	0.48	0.48	0.50	0.49	0.48	0.48	0.49	0.44	0.50	0.50	0.51	0.52	0.51

Table 1. Continued

(b)

Location	Sahneh										Harsin							
Sample	UH-21						UH-8				UH-9							
Mineral No.	Opx 1	Opx 2	Opx 3	Opx 4	Opx 5	Opx 6	Opx 7	Opx 8	Opx 9	Opx 10	Opx 11	Opx 12	Opx 13	Opx 14	Cpx 15	Cpx 16	Cpx 17	Cpx 18
SiO_2	56.41	56.98	56.97	56.45	56.30	56.00	56.04	56.87	56.24	56.01	57.03	55.77	56.84	57.06	52.00	52.74	50.85	52.05
TiO_2	0.047	0.023	0.030	0.042	0.000	0.014	0.000	0.036	0.010	0.016	0.000	0.001	0.046	0.011	0.385	0.258	0.308	0.313
Al_2O_3	3.574	2.928	3.021	3.063	3.045	3.006	3.035	3.073	2.912	2.837	2.942	2.504	2.962	2.997	3.881	3.974	3.899	3.993
Cr_2O_3	0.996	0.924	0.851	0.901	1.015	0.848	0.910	0.936	0.880	0.915	0.763	1.004	0.874	0.956	1.198	1.115	1.223	1.258
FeO	4.015	2.974	4.235	4.945	4.627	4.94	4.945	4.669	4.989	5.009	5.195	5.308	3.954	3.394	2.602	2.426	3.075	2.805
MgO	31.82	33.72	33.19	34.00	33.55	33.21	33.26	32.98	34.01	34.36	34.18	31.62	34.43	32.98	15.38	15.82	16.74	16.31
CaO	2.801	1.923	1.939	1.151	1.745	2.515	2.315	2.840	1.077	1.042	0.649	3.504	0.863	2.826	23.96	23.89	22.73	22.91
Na_2O	0.629	0.046	0.221	0.019	0.020	0.042	0.027	0.031	0.015	0.000	0.000	0.048	0.000	0.029	0.457	0.414	0.324	0.484
K_2O	0.009	0.000	0.000	0.013	0.000	0.008	0.008	0.000	0.000	0.000	0.000	0.001	0.015	0.000	0.014	0.005	0.013	0.015
Total	100.30	99.52	100.45	100.59	100.30	100.59	100.54	101.43	100.13	100.18	100.76	99.75	99.98	100.25	99.87	100.64	99.16	100.14
Cation																		
Si	1.937	1.963	1.952	1.932	1.933	1.920	1.923	1.937	1.932	1.921	1.948	1.941	1.950	1.960	1.900	1.909	1.864	1.890
Ti	0.001	0.001	0.001	0.001	0.000	0.000	0.000	0.001	0.000	0.000	0.000	0.000	0.001	0.000	0.011	0.007	0.008	0.009
Al	0.145	0.119	0.122	0.124	0.123	0.121	0.123	0.123	0.118	0.115	0.118	0.103	0.120	0.121	0.167	0.170	0.168	0.171
Cr	0.027	0.025	0.023	0.024	0.028	0.023	0.025	0.025	0.024	0.025	0.021	0.028	0.024	0.026	0.035	0.032	0.035	0.036
Fe^{3+}	0.000	0.000	0.000	0.000	0.000	0.017	0.009	0.000	0.000	0.017	0.000	0.000	0.000	0.000	0.010	0.000	0.075	0.029
Fe^{2+}	0.115	0.086	0.121	0.142	0.133	0.125	0.133	0.133	0.143	0.126	0.148	0.154	0.113	0.098	0.070	0.073	0.019	0.056
Mg	1.629	1.732	1.695	1.734	1.717	1.698	1.701	1.675	1.742	1.757	1.741	1.640	1.761	1.689	0.838	0.854	0.914	0.883
Ca	0.103	0.071	0.071	0.042	0.064	0.092	0.085	0.104	0.040	0.038	0.024	0.131	0.032	0.104	0.938	0.927	0.893	0.892
Na	0.042	0.003	0.015	0.001	0.001	0.003	0.002	0.002	0.001	0.000	0.000	0.003	0.000	0.002	0.032	0.029	0.023	0.034
Total	4.000	4.000	4.000	4.000	4.000	4.000	4.000	4.000	4.000	4.000	4.000	4.000	4.000	4.000	4.000	4.000	4.000	4.000
Mg#	93.4	95.3	93.3	92.5	93.0	92.3	92.3	92.6	92.4	92.4	92.4	91.3	93.9	94.5	91.3	92.1	90.7	91.2
End-member																		
Wo	5.58	3.76	3.77	2.20	3.35	4.78	4.41	5.42	2.06	1.98	1.24	6.79	1.66	5.50	50.56	49.99	46.95	47.93
En	88.2	91.7	89.8	90.4	89.7	87.9	88.2	87.6	90.5	90.6	91.0	85.2	92.4	89.3	45.2	46.1	48.1	47.5
Fs	6.24	4.54	6.43	7.38	6.94	7.33	7.36	6.96	7.45	7.41	7.76	8.02	5.95	5.16	4.29	3.96	4.96	4.58

Wo=Wollastonite; En=Enstatite; Fs=Ferrosilite.

Table 1. Continued

Location	Sahneh								Harsin											
Sample	UH-21												UH-9							
Mineral No.	Cpx 1	Cpx 2	Cpx 3	Cpx 4	Cpx 5	Cpx 6	Cpx 7	Cpx 8	Cpx 9	Cpx 10	Cpx 11	Cpx 12	Cpx 13	Cpx 14	Cpx 15	Cpx 16	Cpx 17	Cpx 18	Cpx 19	Cpx 20
SiO_2	52.99	52.50	52.08	52.42	52.81	51.34	52.30	52.64	52.30	51.51	52.10	52.47	52.86	51.36	52.20	53.15	53.09	53.46	53.66	52.76
TiO_2	0.435	0.448	0.514	0.518	0.650	0.663	0.993	0.782	1.013	1.149	1.103	0.775	0.933	0.645	0.630	0.383	0.394	0.409	0.458	0.681
Al_2O_3	3.063	3.200	3.173	3.198	3.092	3.813	3.032	3.032	3.114	3.553	3.191	3.017	2.663	4.101	3.918	3.174	3.143	2.767	2.070	2.900
Cr_2O_3	0.828	0.724	0.877	0.756	0.559	0.56	0.098	0.122	0.098	0.119	0.182	0.148	0.308	0.954	0.844	0.774	0.764	0.392	0.495	0.329
FeO	4.593	4.757	4.736	4.699	4.63	5.182	5.289	5.248	5.211	5.139	5.169	5.014	4.872	4.304	4.294	4.611	4.526	4.48	4.356	5.006
MgO	15.77	15.80	15.39	15.42	15.44	16.37	15.88	15.70	15.49	15.41	15.41	15.70	15.43	15.10	15.47	16.79	15.99	16.04	15.95	15.44
MnO	0.118	0.137	0.106	0.145	0.127	0.103	0.198	0.133	0.151	0.126	0.156	0.161	0.187	0.134	0.137	0.135	0.106	0.13	0.104	0.165
CaO	22.06	21.71	22.01	22.47	22.64	20.97	22.14	22.22	22.73	22.26	22.89	22.53	22.70	22.61	22.51	21.35	22.32	22.78	23.31	22.65
Na_2O	0.489	0.441	0.537	0.528	0.504	0.52	0.44	0.395	0.527	0.472	0.483	0.392	0.436	0.496	0.514	0.408	0.477	0.473	0.453	0.456
K_2O	0.014	0.004	0.013	n.d	0.005	n.d.	n.d.	0.004	n.d.	n.d.	0.006	0.005	0.024	n.d.	0.016	0.005	0.013	n.d.	0.003	n.d.
Total	100.36	99.72	99.44	100.16	100.45	99.52	100.39	100.29	100.63	99.76	100.69	100.20	100.42	99.72	100.54	100.78	100.84	100.96	100.85	100.43
Cation																				
Si	1.932	1.926	1.921	1.920	1.926	1.891	1.914	1.925	1.911	1.898	1.904	1.921	1.932	1.891	1.902	1.925	1.927	1.938	1.949	1.929
Ti	0.012	0.012	0.014	0.014	0.018	0.018	0.027	0.022	0.028	0.032	0.030	0.021	0.026	0.018	0.017	0.010	0.011	0.011	0.013	0.019
Al	0.132	0.138	0.138	0.138	0.133	0.166	0.131	0.131	0.134	0.154	0.137	0.130	0.115	0.178	0.168	0.135	0.134	0.118	0.089	0.125
Cr	0.024	0.021	0.026	0.022	0.016	0.016	0.003	0.004	0.003	0.003	0.005	0.004	0.009	0.028	0.024	0.022	0.022	0.011	0.014	0.010
Fe^{3+}	0.000	0.000	0.005	0.009	0.000	0.036	0.016	0.001	0.022	0.017	0.022	0.008	0.000	0.013	0.005	0.000	0.002	0.006	0.006	0.002
Fe^{2+}	0.140	0.146	0.146	0.130	0.141	0.105	0.138	0.160	0.126	0.133	0.125	0.141	0.149	0.113	0.123	0.139	0.134	0.127	0.124	0.149
Mg	0.857	0.864	0.846	0.842	0.840	0.899	0.866	0.856	0.844	0.846	0.840	0.857	0.840	0.829	0.840	0.906	0.865	0.867	0.864	0.841
Ca	0.861	0.854	0.870	0.882	0.885	0.828	0.868	0.871	0.890	0.879	0.897	0.884	0.889	0.892	0.879	0.828	0.868	0.885	0.907	0.887
Na	0.035	0.031	0.038	0.037	0.036	0.037	0.031	0.028	0.037	0.034	0.034	0.028	0.031	0.035	0.036	0.029	0.034	0.033	0.032	0.032
Total	3.131	3.139	3.134	3.113	3.110	3.168	3.126	3.126	3.105	3.117	3.098	3.111	3.101	3.104	3.117	3.167	3.128	3.111	3.090	3.107
Mg#	86.0	85.5	85.3	85.4	85.6	84.9	84.3	84.2	84.1	84.2	84.2	84.8	84.9	86.2	86.5	86.6	86.3	86.4	86.7	84.6
End-member																				
Wo	46.3	45.8	45.8	47.2	47.4	43.9	45.8	46.1	47.0	46.7	47.3	46.7	47.3	48.1	47.5	44.2	46.4	46.9	47.7	47.2
En	46.1	46.4	46.4	45.1	45.0	47.7	45.7	45.4	44.6	44.9	44.3	45.2	44.7	44.7	45.4	48.4	46.2	45.9	45.4	44.7
Fs	7.53	7.83	7.83	7.70	7.57	8.46	8.54	8.51	8.41	8.41	8.34	8.11	7.93	7.15	7.07	7.45	7.35	7.20	6.95	8.14

Wo=Wollastonite; En=Enstatite; Fs=Ferrosilite.
n.d.= not detected.

Table 1. Continued

(c)

Location	Sahneh							Harsin												
Sample	UH-21							UH-8								UH-9				
Mineral Points	Ol 1	Ol 2	Ol 3	Ol 4	Ol 5	Ol 6	Ol 7	Ol 8	Ol 9	Ol 10	Ol 11	Ol 12	Ol 13	Ol 14	Ol 15	Ol 16	Ol 17	Ol 18	Ol 19	Ol 20
SiO_2	41.51	42.37	41.87	41.60	41.26	41.99	43.60	42.43	40.87	41.16	43.91	40.57	40.95	40.42	42.36	40.26	42.21	40.80	40.51	40.37
TiO_2	0.000	0.000	0.011	0.011	0.032	0.027	0.000	0.000	0.013	0.000	0.000	0.015	0.000	0.000	0.028	0.000	0.022	0.000	0.00	0.000
Al_2O_3	0.000	0.021	0.006	0.004	0.026	0.000	0.100	0.050	0.113	0.000	0.073	0.029	0.198	0.115	0.040	0.087	0.011	0.195	0.000	0.021
Cr_2O_3	0.048	0.000	0.036	0.034	0.000	0.012	0.006	0.000	0.000	0.027	0.009	0.000	0.000	0.000	0.012	0.000	0.014	0.080	0.048	0.000
FeO	10.13	10.38	10.48	10.12	8.373	9.180	4.746	8.320	8.472	6.781	6.671	7.433	8.243	8.095	7.963	5.833	8.966	6.899	10.133	10.377
MgO	49.68	49.65	49.06	50.15	50.07	48.38	50.67	48.77	50.03	50.40	48.54	51.26	49.68	51.31	49.13	53.11	47.57	50.54	49.68	49.65
CaO	0.048	0.091	0.055	0.055	0.074	0.039	0.083	0.131	0.133	0.074	0.298	0.137	0.063	0.259	0.125	0.038	0.137	0.064	0.05	0.091
Na_2O	0.021	0.007	0.000	0.005	0.008	0.000	0.013	0.009	0.008	0.000	0.008	0.016	0.021	0.022	0.001	0.000	0.031	0.000	0.021	0.007
K_2O	0.017	0.007	0.015	0.011	0.012	0.009	0.015	0.004	0.025	0.013	0.007	0.003	0.000	0.030	0.011	0.004	0.006	0.018	0.017	0.007
NiO	0.159	0.144	0.139	0.124	0.619	0.281	0.207	0.528	0.448	0.388	0.065	0.567	0.499	0.406	0.261	0.307	0.433	0.456	0.159	0.144
(OH)	0.000	0.000	0.000	0.000	0.00	0.00	0.00	0.00	0.00	0.00	0.00	0.00	0.00	0.00	0.00	0.00	0.00	0.00	0.00	0.00
Total	101.614	102.662	101.675	102.112	100.47	99.91	99.44	100.24	100.11	98.84	99.58	100.03	99.65	100.65	99.93	99.64	99.40	99.05	100.61	100.66
Cation																				
Si	1.003	1.015	1.014	0.999	1.006	1.034	1.061	1.041	0.998	1.012	1.077	0.986	1.005	0.977	1.038	0.970	1.048	1.001	1.00	1.015
Ti	0.000	0.000	0.000	0.000	0.001	0.000	0.000	0.000	0.000	0.000	0.000	0.000	0.000	0.000	0.001	0.000	0.000	0.000	0.000	0.000
Al	0.000	0.001	0.000	0.000	0.001	0.000	0.003	0.001	0.003	0.000	0.002	0.001	0.006	0.003	0.001	0.002	0.000	0.006	0.000	0.001
Cr	0.001	0.000	0.001	0.001	0.000	0.000	0.000	0.000	0.000	0.001	0.000	0.000	0.000	0.000	0.000	0.000	0.000	0.002	0.001	0.000
Fe^{3+}	0.000	0.000	0.000	0.001	0.000	0.000	0.000	0.000	0.000	0.000	0.000	0.026	0.000	0.043	0.000	0.057	0.000	0.000	0.000	0.000
Fe^{2+}	0.205	0.208	0.212	0.202	0.171	0.189	0.097	0.171	0.173	0.139	0.137	0.125	0.169	0.121	0.163	0.061	0.186	0.142	0.205	0.208
Mg	1.790	1.774	1.771	1.795	1.820	1.776	1.838	1.784	1.822	1.847	1.776	1.858	1.818	1.849	1.794	1.908	1.761	1.849	1.790	1.774
Ca	0.001	0.002	0.001	0.001	0.002	0.001	0.002	0.003	0.003	0.002	0.008	0.004	0.002	0.007	0.003	0.001	0.004	0.002	0.001	0.002
Total	3.000	3.000	3.000	3.000	3.000	3.000	3.000	3.000	3.000	3.000	3.000	3.000	3.000	3.000	3.000	3.000	3.000	3.000	3.000	3.000
End-member																				
Fo	89.7	89.4	89.2	89.8	91.3	90.3	94.9	91.1	91.2	92.9	92.5	92.3	91.4	91.6	91.5	94.2	90.3	92.8	89.7	89.4
Fa	10.3	10.5	10.7	10.2	8.6	9.6	4.99	8.7	8.7	7.01	7.13	7.5	8.5	8.1	8.32	5.8	9.5	7.11	10.3	10.5

Fo=Forsterite; Fa= Fayalite.

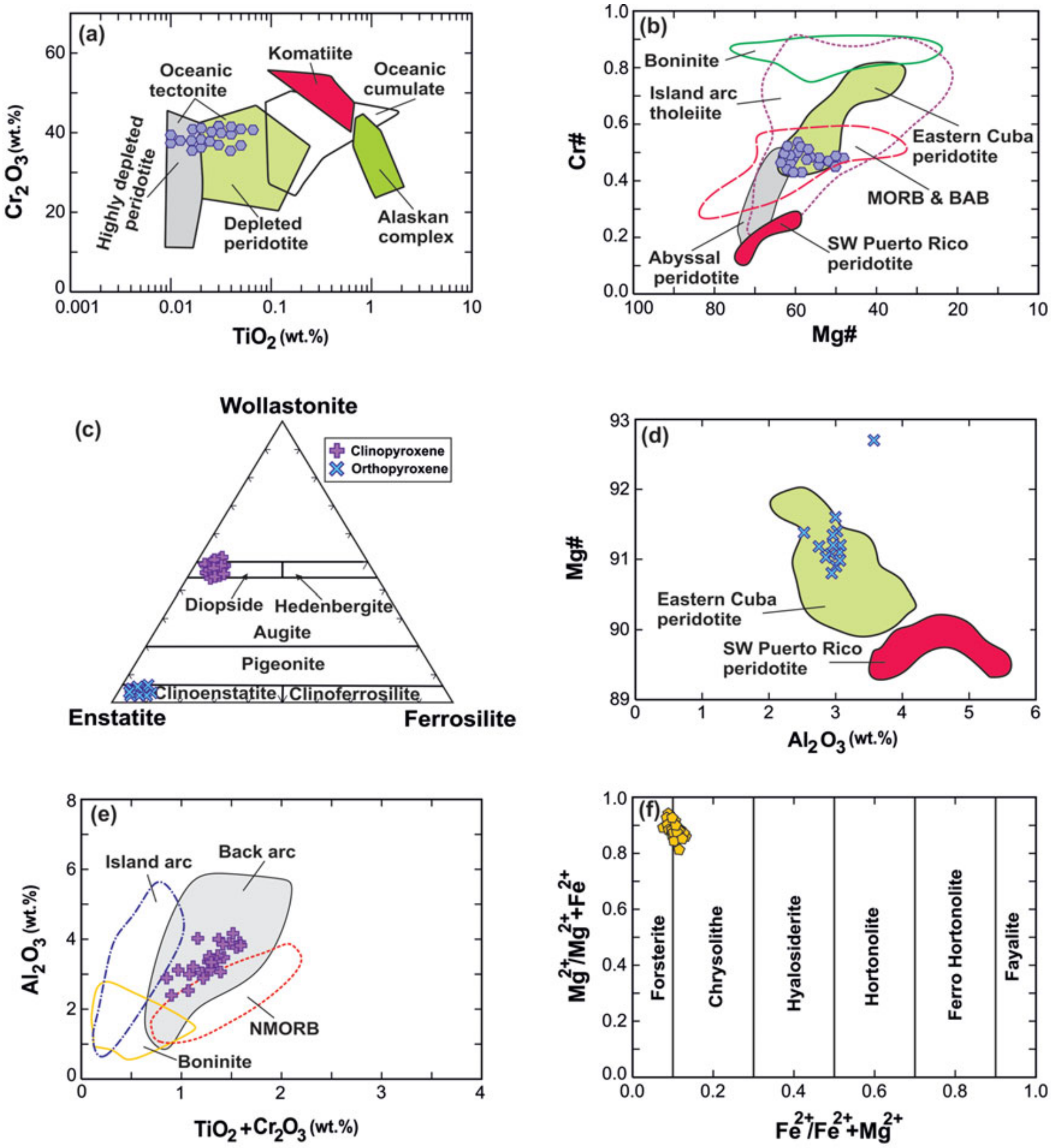

Figure 5. (Colour online) (a) Diagram of Cr_2O_3 versus TiO_2 in spinel. Fields for ultramafic rocks are after Herbert (1982), Jan & Windley (1990) and Zhou & Kerrich (1992). (b) Mg# versus Cr# diagram for spinel. Fields of spinel compositions in abyssal peridotite, MORB-BAB, island arc tholeiite and boninite are from Dick & Bullen (1984) and the GEOROC database. Data of spinel in eastern Cuba dunites and harzburgites are from Marchesi *et al.* (2006), and those in SW Puerto Rico lherzolites are from Marchesi *et al.* (2011). (c) Classification of pyroxenes (Morimoto, 1988). (d) Diagram of Al_2O_3 (wt %) versus Mg# in orthopyroxene. Data of orthopyroxene in eastern Cuba dunites and harzburgite are from Marchesi *et al.* (2006), and those in SW Puerto Rico lherzolites are from Marchesi *et al.* (2011). (e) $TiO_2 + Cr_2O_3$ (wt %) versus Al_2O_3 (wt %) diagram (after Hout *et al.* 2002) for clinopyroxene. Fields are outlined for clinopyroxene compositions in boninite (Van der Laan *et al.* 1992), island arc tholeiite and back-arc basalt (Hawkins & Allen, 1994) and NMORB (Stakes & Franklin, 1994). (f) Classification of olivine minerals (Deer, Howie & Zussman, 1992).

mainly indicate that all of the HSP samples have experienced moderate to low degrees of serpentinization (Table 2). They are characterized by low contents of SiO_2 (38.8–43.5 wt %), Al_2O_3 (0.0–3.8 wt %) and CaO (0.2–8.2 wt %). Al_2O_3 mainly resides in spinel and is partly incorporated in primary pyroxene (Li *et al.* 2015). The samples display variable degrees of depletion, with MgO contents ranging from 31.1 to 45.9 wt %. In addition, their trace element abundances are highly variable. These samples have variable contents of Cr (96–7560 ppm) and Ni (112–2880 ppm). Most of their Cr and Ni contents are higher than those of the primitive mantle (Ni = 2090 ppm and Cr = 3240 ppm; Hart & Zindler, 1986), which probably reflects their high olivine/pyroxene ratios and relatively high Cr-spinel contents (Whattam, Cho & Smith, 2011).

On the MgO/SiO_2 versus Al_2O_3/SiO_2 diagram (Fig. 6), most of the peridotites plot at low Al_2O_3/SiO_2 values (<0.04). The most depleted (refractory) compositions are defined by Al_2O_3/SiO_2 and MgO/SiO_2 ratios of <0.01 and >1, respectively (Jagoutz *et al.* 1979;

Table 2. Chemical compositions of the HSP

Sample Rock type Location	UH-3 Lhz Harsin	UH-5 Cpx-hz Harsin	UH-8 Du Harsin	UH-9 Hz Harsin	UH-10 Hz Sahneh	UH-17 Du Harsin	UH-19 Cpx-hz Sahneh	UH-20 Lhz Sahneh
SiO_2 (wt %)	43.54	43.45	42.11	38.81	41.13	40.80	42.94	41.86
TiO_2	0.04	0.04	0.02	0.02	0.02	0.01	0.01	0.06
Al_2O_3	1.32	1.03	0.93	3.47	3.18	0.34	1.39	3.81
Fe_2O_3	11.17	9.74	9.04	9.70	7.74	9.43	9.81	12.39
MnO	0.17	0.16	0.11	0.11	0.11	0.13	0.15	0.18
MgO	33.97	37.96	44.02	44.37	38.69	45.97	42.35	31.09
CaO	4.28	5.91	0.58	0.52	1.54	0.62	1.90	5.22
Na_2O	0.13	0.14	0.07	0.07	0.08	0.03	0.05	0.10
K_2O	0.00	0.00	0.03	0.09	0.03	0.00	0.00	0.00
P_2O_5	0.007	0.007	0.014	0.017	0.014	0.006	0.007	0.007
Cr_2O_3	0.62	0.57	0.44	0.59	0.95	0.58	0.59	0.47
NiO	0.18	0.17	0.36	0.34	0.26	0.34	0.33	0.15
LOI	4.45	1.35	2.66	1.78	6.56	2.06	0.97	4.80
Total	99.87	100.50	100.32	99.75	100.06	100.31	100.48	100.13
Sc (ppm)	18.2	20.1	5.57	5.71	4.46	9.09	13.0	20.2
V	75.0	83.4	18.7	35.8	18.8	39.9	61.2	59.2
Cr	4240	3900	2980	4030	6470	4000	4010	3230
Co	95.9	87.4	99.6	108	96.5	122	106	113
Ni	1410	1340	2840	2710	2060	2670	2590	1160
Cu	15.3	15.3	2.73	319	14.0	9.19	30.0	13.7
Zn	47.3	44.1	38.6	36.9	34.4	44.0	48.0	57.5
Ga	1.82	1.73	0.614	4.44	2.76	0.67	1.64	2.81
Rb	0.559	0.670	0.912	1.82	0.425	0.460	1.24	1.17
Sr	4.59	6.49	5.67	10.8	4.18	4.96	2.20	7.90
Zr	0.834	1.30	0.845	1.95	1.31	0.195	0.164	0.436
Nb	0.076	0.105	0.082	0.158	0.057	0.019	0.038	n.d
Cs	0.022	0.022	0.036	0.119	0.013	0.006	0.018	0.029
Ba	3.36	4.22	2.00	6.38	1.33	0.497	0.632	0.656
Pb	0.147	0.241	0.164	0.372	0.120	0.066	0.128	0.106
Th	0.022	0.036	0.027	0.116	0.020	0.003	0.090	0.052
U	0.032	0.020	0.005	0.073	0.005	0.002	0.008	0.007
Hf	0.029	0.042	0.022	0.062	0.035	0.004	0.005	0.024
Ta	0.013	0.018	0.009	0.034	0.010	0.004	0.026	0.009
Y	0.913	1.15	0.411	0.321	0.343	0.200	0.541	0.875
La (ppm)	0.092	0.161	0.320	0.417	0.099	0.145	0.529	0.289
Ce	0.166	0.298	0.500	0.880	0.236	0.200	0.594	0.438
Pr	0.020	0.037	0.060	0.100	0.034	0.023	0.073	0.054
Nd	0.087	0.160	0.243	0.396	0.155	0.086	0.230	0.231
Sm	0.033	0.049	0.054	0.075	0.048	0.018	0.036	0.079
Eu	0.013	0.022	0.012	0.019	0.028	0.003	0.009	0.037
Gd	0.072	0.098	0.062	0.067	0.057	0.024	0.046	0.121
Tb	0.017	0.022	0.011	0.010	0.009	0.004	0.009	0.024
Dy	0.159	0.192	0.073	0.061	0.064	0.032	0.085	0.173
Ho	0.042	0.051	0.016	0.014	0.015	0.008	0.022	0.035
Er	0.146	0.170	0.049	0.044	0.043	0.025	0.074	0.098
Tm	0.023	0.028	0.008	0.008	0.006	0.004	0.013	0.014
Yb	0.177	0.201	0.056	0.073	0.046	0.031	0.095	0.083
Lu	0.028	0.031	0.009	0.014	0.008	0.005	0.015	0.011
Mg#	85.8	88.5	90.6	90.1	90.8	90.6	89.5	83.2

Hart & Zindler, 1986). Thus, peridotites of residual mantle origin should follow a progressive trend toward lower Al_2O_3/SiO_2 values (reflecting a higher degree of melt extraction) and higher MgO/SiO_2 values along a trend that parallels the terrestrial array (Fig. 6). The HSP rocks show a trend extending from the peridotites, which have more fertile $Al_2O_3/SiO_2 = 0.07–0.09$ and $MgO/SiO_2 = 1.1–1.14$, to more refractory peridotite ($Al_2O_3/SiO_2 = 0.00–0.05$ and $MgO/SiO_2 = 0.75–1.1$); they all plot along or above the terrestrial array. Their high MgO/SiO_2 values reflect their higher olivine/pyroxene ratios. Some samples (UH-28 and UH-30) record low Al_2O_3/SiO_2 values ($\sim$0.00), reflecting their more depleted (refractory) compositions; they are not plotted. On this diagram (Fig. 6), some samples show lower values of MgO/SiO_2 and Al_2O_3/SiO_2, indicating that they have experienced MgO loss or SiO_2 addition relative to normal mantle melting residues (Marchesi *et al.* 2013).

Most of these rocks have REE patterns that are sub-parallel to each other (Fig. 7a), although two samples exhibit REE patterns that are accompanied by slightly bulged shapes around their MREE segments. All of the peridotite samples are characterized by variously depleted REE patterns compared to the depleted MORB mantle (DMM), and their total REE contents range from 0.5 to 6.2 ppm. The presence of slightly positive Eu anomalies in some samples (Niu, Langmuir & Kinzler, 1997) is due to reactions with plagioclase-bearing rocks, such as oceanic gabbro (e.g. Klinkhammer *et al.* 1994; Douville *et al.* 2002; Chen *et al.* 2013). Recent experimental studies demonstrate that the chlorinity

Table 2. Continued

Sample Rock type Location	UH-21 Cpx-hz Sahneh	UH-22 Cpx-hz Sahneh	UH-23 Cpx-hz Sahneh	UH-24 Du Sahneh	UH-26 Cpx-hz Harsin	UH-28 Cpx-hz Harsin	UH-30 Cpx-hz Sahneh	UH-31 Cpx-hz Sahneh
SiO_2 (wt %)	39.24	39.01	43.48	43.36	41.04	41.53	39.85	39.21
TiO_2	0.01	0.01	0.01	0.01	0.01	0.02	0.02	0.06
Al_2O_3	2.87	0.06	0.22	0.43	0.16	0.00	0.00	0.06
Fe_2O_3	9.84	10.84	8.09	9.08	10.06	10.30	10.93	10.85
MnO	0.14	0.15	0.18	0.13	0.15	0.14	0.13	0.14
MgO	40.92	42.52	35.48	43.23	43.87	44.29	42.58	43.25
CaO	3.00	0.82	8.18	0.93	1.52	0.96	0.49	0.56
Na_2O	0.01	0.11	0.04	0.02	0.10	0.09	0.09	0.18
K_2O	0.00	0.00	0.01	0.00	0.00	0.00	0.00	0.00
P_2O_5	0.008	0.004	0.007	0.006	0.004	0.004	0.005	0.010
Cr_2O_3	0.082	1.10	0.36	0.57	0.66	0.61	0.41	0.55
NiO	0.15	0.37	0.07	0.32	0.35	0.35	0.35	0.33
LOI	4.36	6.45	4.35	2.45	2.18	1.98	5.23	5.03
TOTAL	100.63	101.43	100.45	100.52	100.10	100.27	100.07	100.22
Sc (ppm)	6.23	8.92	15.7	9.60	10.1	9.67	7.11	10.8
V	10.9	32.4	45.2	33.9	42.6	39.2	30.6	35.0
Cr	562	7560	2450	3890	4520	4200	2780	3770
Co	118	108	64.3	92.8	103	106	101	91.4
Ni	1140	2880	573	2530	2720	2760	2730	2630
Cu	136	3.65	2.26	6.38	21.5	13.8	2.74	11.2
Zn	38.9	40.3	40.1	35.9	43.7	44.8	35.0	34.1
Ga	1.18	0.688	0.717	0.557	0.841	0.726	0.705	1.75
Rb	0.670	0.724	1.24	0.621	0.488	0.290	0.223	0.634
Sr	30.4	0.346	27.2	5.50	0.334	0.127	3.21	48.6
Zr	0.085	0.167	0.099	0.071	0.326	0.098	0.980	3.20
Nb	n.d	0.039	0.004	0.004	0.083	0.039	0.075	0.375
Cs	0.018	0.008	0.267	0.041	0.005	0.003	0.006	0.025
Ba	3.12	0.264	2.24	1.22	0.182	0.105	0.62	2.58
Pb	0.471	0.088	0.051	0.131	0.096	0.072	0.051	0.155
Th	0.019	0.015	0.014	0.005	0.015	0.006	0.023	0.033
U	0.005	0.006	0.004	0.002	0.005	0.004	0.006	0.015
Hf	0.005	0.006	0.004	0.003	0.012	0.003	0.027	0.098
Ta	0.010	0.012	0.012	0.008	0.038	0.008	0.009	0.033
Y	0.653	0.247	0.217	1.29	0.282	0.117	0.191	1.53
La (ppm)	0.820	0.528	0.192	1.25	0.026	0.006	0.062	0.434
Ce	1.26	0.811	0.227	2.21	0.050	0.012	0.134	0.969
Pr	0.133	0.077	0.028	0.282	0.006	0.001	0.017	0.127
Nd	0.485	0.247	0.098	1.19	0.027	0.005	0.079	0.593
Sm	0.102	0.045	0.022	0.264	0.009	0.001	0.019	0.167
Eu	0.056	0.007	0.003	0.084	0.006	0.001	0.008	0.084
Gd	0.118	0.043	0.031	0.295	0.019	0.004	0.026	0.218
Tb	0.019	0.006	0.005	0.044	0.005	0.001	0.004	0.037
Dy	0.128	0.043	0.042	0.274	0.041	0.013	0.033	0.251
Ho	0.026	0.010	0.009	0.052	0.011	0.004	0.008	0.056
Er	0.076	0.032	0.026	0.124	0.043	0.020	0.028	0.160
Tm	0.011	0.005	0.004	0.012	0.009	0.004	0.005	0.024
Yb	0.079	0.041	0.033	0.055	0.064	0.040	0.044	0.165
Lu	0.012	0.007	0.005	0.008	0.012	0.008	0.008	0.025
Mg#	89.2	88.6	89.7	90.4	89.6	89.5	88.5	88.8

and redox potential of the fluid is a major controlling factor on LREE and Eu mobility (Allen & Seyfried, 2005; Paulick *et al.* 2006; Deschamps *et al.* 2013) and that the presence of plagioclase is not required for the generation of LREE-enriched fluid compositions with positive Eu anomalies.

The abundances of incompatible trace elements on the primitive mantle-normalized diagram (Fig. 7b) show elevated abundances of U, Pb, Sr, Cs and Rb and small negative Ba and Zr anomalies compared to their neighbouring elements. Except for a few elements, such as Cs, Pb and Sr, in some samples, the trace element contents in the HSP samples are depleted compared to those of the primitive mantle (Sun & McDonough, 1989). This feature suggests the residual mantle origin of their protolith. Assessing the abundances of the incompatible trace elements normalized to the primitive mantle (Fig. 7b) reveals that some samples show a decoupling between Nb and Ta and are more enriched in Ta. This is consistent with depleted peridotites from abyssal and continental passive margins, whereas two samples show higher depletion on MREE and HREE compared to abyssal peridotites and the REE patterns reaching up to the field of typical supra-subduction peridotites (Parkinson & Pearce, 1998; Uysal *et al.* 2016).

7. Sr–Nd isotopic ratios

The $^{87}Sr/^{86}Sr$ and $^{143}Nd/^{144}Nd$ isotopic ratios of the HSP rocks are shown in Table 3. Their initial ratios are calculated based on an age of 80 Ma, which

Table 2. Continued

Sample Rock type Location	UH-42 Cpx-hz Sahneh	UH-46 Lhz Sahneh	UH-53 Cpx-hz Harsin	SH1 Du Harsin	SH2 Du Harsin	SH3 Du Harsin	TB2 Du Harsin	UM1 Du Harsin
SiO_2 (wt %)	41.35	42.62	41.07	40.1	41.1	40.6	40.5	40.0
TiO_2	0.04	0.01	0.02	0.01	0.01	0.01	0.02	0.03
Al_2O_3	1.37	3.70	1.87	0.37	1.08	0.62	1.14	1.15
Fe_2O_3	10.52	10.52	10.77	8.86	9.21	8.51	7.62	8.77
MnO	0.10	0.11	0.18	0.11	0.12	0.12	0.08	0.12
MgO	45.17	35.17	41.33	43.5	45.9	45.5	45.9	44.3
CaO	0.29	1.01	0.26	0.62	1.29	0.72	0.23	1.12
Na_2O	0.09	0.03	0.03	0.02	0.02	0.03	0.06	0.06
K_2O	0.00	0.00	0.00	0.01	0.01	0.01	0.02	0.01
P_2O_5	0.011	0.008	0.009	0.010	0.010	0.010	nd	nd
Cr_2O_3	*	*	*	0.39	0.32	0.45	0.36	0.39
NiO	*	*	*	*	*	*	*	*
LOI	1.24	6.83	4.59	6.82	1.29	3.34	4.20	3.82
TOTAL	100.18	100.01	100.13	100.82	100.36	99.92	100.11	99.76
Sc (ppm)	*	*	*	*	*	*	*	*
V	32.7	2.57	20.5	5	5	5	n.d.	n.d.
Cr	651	95.6	3630	2590	2200	3030	2490	2900
Co	13.9	15.6	126	102	119	111	96.5	110
Ni	112	161	1390	2150	2380	2260	2080	2110
Cu	41.1	25.6	3.35	5	8	5	5	13
Zn	10.2	11.0	72.4	43	52	47	40	52
Ga	12.0	12.5	2.89	0.5	1.1	0.8	16	1.4
Rb	0.854	0.105	0.893	0.2	0.2	0.3	0.4	0.9
Sr	202	178	3.54	6.7	2.9	0.9	9.2	5.6
Zr	1.52	0.359	1.28	n.d	n.d	n.d	2	3
Nb	0.205	0.095	0.186	0.2	0.2	0.2	n.d	n.d
Cs	0.131	0.026	0.020	0.01	0.01	0.01	0.07	0.02
Ba	4.46	5.17	1.31	2.1	5.1	1.8	2.7	2.2
Pb	0.176	0.145	0.221	5	5	5	n.d	n.d
Th	0.230	0.176	0.051	0.05	0.05	0.05	0.06	0.05
U	0.018	0.001	0.007	0.05	0.05	0.05	n.d	n.d
Hf	0.052	0.003	0.036	0.2	0.2	0.2	n.d	n.d
Ta	0.134	0.031	0.018	n.d	n.d	n.d	n.d	n.d
Y	1.24	0.099	0.289	0.5	0.5	0.5	0.8	0.1
La (ppm)	0.256	0.152	0.130	0.5	0.5	0.5	0.7	n.d
Ce	0.627	0.231	0.254	0.5	0.5	0.5	0.9	n.d
Pr	0.070	0.034	0.033	0.03	0.03	0.03	0.15	n.d
Nd	0.345	0.148	0.145	0.1	0.1	0.1	0.7	0.2
Sm	0.126	0.029	0.036	0.03	0.03	0.03	n.d	0.08
Eu	0.129	0.112	0.011	0.03	0.03	0.03	0.1	n.d
Gd	0.200	0.030	0.043	0.05	0.05	0.05	0.09	n.d
Tb	0.036	0.004	0.008	0.01	0.01	0.01	n.d	n.d
Dy	0.247	0.021	0.047	0.05	0.05	0.05	0.1	0.07
Ho	0.050	0.004	0.011	0.01	0.02	0.01	0.02	0.02
Er	0.141	0.009	0.021	0.03	0.03	0.03	0.05	0.06
Tm	0.020	0.001	0.004	0.01	0.01	0.01	0.01	n.d
Yb	0.119	0.007	0.020	0.05	0.06	0.04	0.11	0.11
Lu	0.017	0.001	0.004	0.01	0.01	0.01	0.01	0.02
Mg#	88.6	86.9	88.4	90.7	90.8	91.4	92.3	90.9

*=not measured; .d.=not detected.

Aziz, Elias & Aswad (2011) reported from neighbouring Penjween serpentinized peridotites using the Rb–Sr method (80-100 Ma). Braud (1978) and Shahidi & Nazari (1997) have suggested a Jurassic to Late Cretaceous age for the Harsin–Sahneh ophiolite complex based on its tectonic and stratigraphic relationships. Their $^{87}Sr/^{86}Sr_{(i=initial)}$ and $^{143}Nd/^{144}Nd_{(i)}$ ratios range from 0.7038 to 0.7109 and from 0.51214 to 0.51285, respectively. Their $\varepsilon Nd_{(t)}$ values range from –7.5 to +7.8 (Table 3), thus reflecting the contribution of continental material to the source of the HSP rocks. The $^{87}Sr/^{86}Sr_{(i)}$ ratios of the HSP rocks are significantly more radiogenic compared to MORB (0.7025), whereas the $^{143}Nd/^{144}Nd_{(i)}$ ratios of the HSP rocks are lower than that of MORB (0.51315). This suggests that the HSP rocks originated from a depleted mantle source that was affected by alteration reactions (as indicated by their high $^{87}Sr/^{86}Sr_{(i)}$ ratios).

On the $^{87}Sr/^{86}Sr_{(i)}$ versus $\varepsilon Nd_{(t)}$ diagram, the samples plot near the mantle array, and they extend from the MORB (mid-oceanic ridge) field toward the EMII (continental sediments associated with a subducting slab) field and a seawater component (Fig. 8a, b, c). These diagrams show that the HSP rocks were not strongly affected by seawater alteration and the HSP rocks were altered by seawater along deep faults and fractures in an extensional basin. In Figure 8a, the HSP rocks exhibit minor overlapping with the Harsin ophiolite domain due to their highly radiogenic Sr isotopic compositions and less radiogenic Nd isotopic

Table 3. Rb–Sr and Sm–Nd isotopic compositions of the HSP rocks

Sample	Rb	Sr	^{87}Rb/ ^{86}Sr	^{87}Sr/ ^{86}Sr$_{(p)}$	± 1SE	^{87}Sr/ ^{86}Sr$_{(i)}$	Nd	Sm	^{147}Sm/ ^{144}Nd	^{143}Nd/ ^{144}Nd$_{(p)}$	± 1SE	^{143}Nd/ ^{144}Nd$_{(i)}$	εNd (t)	f(Sm/ Nd)	f(Rb/ Sr)	W/R(Closed-system)	W/R(Open-system)
UH-3	0.559	4.59	0.353	0.707533	0.000008	0.70750	0.087	0.033	0.228	0.512536	0.000045	0.51243	− 1.8	0.16	3.26	2.27	1.05
UH-5	0.670	6.49	0.299	0.706848	0.000006	0.70682	0.160	0.049	0.185	0.512680	0.000008	0.51260	1.4	− 0.06	2.61	1.37	0.78
UH-8	0.912	5.67	0.466	0.707518	0.000006	0.70747	0.243	0.054	0.134	0.512729	0.000006	0.51267	2.8	− 0.32	4.63	2.24	1.05
UH-9	1.82	10.8	0.486	0.706975	0.000008	0.70693	0.396	0.075	0.115					− 0.42	4.88	1.50	0.83
UH-10	0.425	4.18	0.294	0.704422	0.000007	0.70439	0.155	0.048	0.186					− 0.06	2.56	0.28	0.24
UH-17	0.460	4.96	0.268	0.706068	0.000007	0.70604	0.086	0.018	0.126	0.512721	0.000023	0.51266	2.8	− 0.36	2.24	0.83	0.56
UH-19	1.24	2.20	1.64	0.704040	0.000006	0.70388	0.230	0.036	0.094	0.512534	0.000036	0.51249	− 0.6	− 0.52	18.8	0.20	0.18
UH-20	1.17	7.90	0.429	0.705991	0.000008	0.70595	0.231	0.079	0.206	0.512817	0.000009	0.51272	3.9	0.05	4.18	0.79	0.54
UH-21	0.670	30.4	0.064	0.706151	0.000006	0.70614	0.485	0.102	0.128	0.512244	0.000013	0.51219	− 6.6	− 0.35	− 0.23	0.88	0.58
UH-22	0.724	0.346	6.05	0.707899	0.000010	0.70730	0.247	0.045	0.111	0.512524	0.000062	0.51247	− 1.0	− 0.44	72.2	3.15	1.25
UH-23	1.24	27.2	0.132	0.708067	0.000006	0.70805	0.098	0.022	0.134					− 0.32	0.59	3.75	1.36
UH-24	0.621	5.50	0.327	0.706849	0.000006	0.70682	1.19	0.264	0.134					− 0.32	2.95	1.37	0.79
UH-26*	0.296	0.816	1.05	0.707734	0.000013	0.70763	0.027	0.009	0.210	0.512939	0.000004	0.51284	6.3	0.07	11.7	2.70	1.15
UH-28*	0.093	0.115	2.34	0.708523	0.000017	0.70829	0.005	0.001	0.173	0.512938	0.000005	0.51286	6.6	− 0.12	27.3	6.98	1.77
UH-30*	0.223	3.21	0.201	0.710931	0.000006	0.71091	0.079	0.019	0.146	0.512451	0.000004	0.51238	− 2.7	− 0.26	1.43		
UH-31*	0.634	48.6	0.038	0.706272	0.000006	0.70627	0.593	0.167	0.170	0.512788	0.000004	0.51271	3.7	− 0.13	− 0.54	0.95	0.62
UH-42	0.854	202	0.012	0.703578	0.000006	0.70358	0.345	0.126	0.221	0.513024	0.000008	0.51292	7.8	0.13	− 0.85	0.12	0.11
UH-46	0.105	178	0.002	0.702887	0.000006	0.70289	0.148	0.029	0.120	0.512868	0.000029	0.51281	5.7	− 0.39	− 0.98	0.02	0.02
UH-53	0.893	3.54	0.730	0.705875	0.000005	0.70580	0.145	0.036	0.149	0.512826	0.000018	0.51276	4.6	− 0.24	7.83	0.74	0.52
SH1*	0.140	0.86	0.469	0.709211	0.000014	0.70916	0.100	0.030	0.181	0.512222	0.000027	0.51214	− 7.5	− 0.08	4.68		
UM1	0.900	5.60	0.465	0.706443	0.000006	0.70640	0.200	0.080	0.242					0.23	4.6	1.05	0.66

The natural Nd and Sr isotope ratios were normalized based on^{146}Nd/^{144}Nd = 0.7219 and ^{86}Sr/^{88}Sr = 0.1194. Averages and1σ for isotope ratio standards, JNdi-1 and NBS987, are ^{143}Nd/^{144}Nd = 0.512119 ± 0.000005 (n = 3) and ^{87}Sr/^{86}Sr = 0.710253 ± 0.000007 (n = 10). The CHUR (Chondritic Uniform Reservoir) values,^{147}Sm/^{144}Nd = 0.1967 and ^{143}Nd/^{144}Nd = 0.512638, were used to calculate the ε^0 (DePaolo & Wasserburg,1976). $f_{(Sm/Nd)} = [(^{147}Sm/^{144}Nd)_{sample}/(^{147}Sm/^{144}Nd)_{CHUR}] - 1$ and $f_{(Rb/Sr)} = [(^{87}Rb/^{86}Sr)_{sample}/(^{87}Rb/^{86}Sr)_{CHUR}] - 1$.

* Rb, Sr, Sm, Nd and ^{87}Sr/86Sr$_{(p)}$ ^{143}Nd/144Nd$_{(p)}$ were measured by isotope dilution method. i=initial and p=present.

W/R(Closed system) = $[(\varepsilon_r^{\,i} - \varepsilon_r^{\,f})/(\varepsilon_r^{\,f}\text{-} - \varepsilon_w^{\,i})] \times (X_r/X_w)$. W/R(Open system) = $(X_r/X_m) \times \ln[(\varepsilon_r^{\,i} - \varepsilon_r^{\,f})/(\varepsilon_r^{\,f} - \varepsilon_w^{\,i}) + 1]$. $\varepsilon_r^{\,i}$ = initial $^{87/86}$Sr (0.702689) for mantle peridotite, element composition X_r as 6.1 ppm for mantle peridotites (Workman & Hart, 2005), $\varepsilon_r^{\,f}$ is the final ^{87}Sr/^{86}Sr of Harsin–Sahneh peridotites, $\varepsilon_w^{\,i}$ is the initial ^{87}Sr/^{86}Sr of hydrothermal fluid as 0.70916, with the element composition of seawater X_w as 8 ppm for present North Atlantic seawater (Palmer & Edmond, 1989).

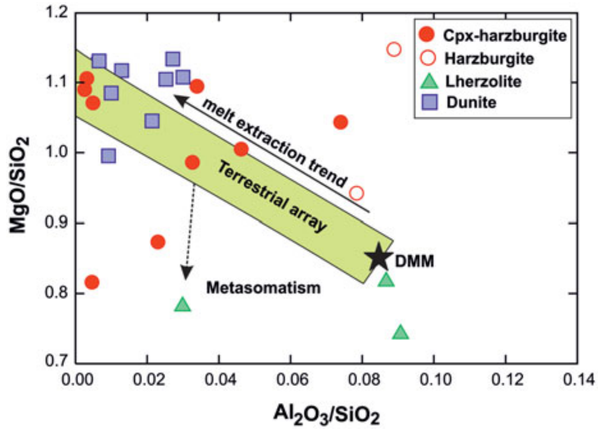

Figure 6. (Colour online) Plot of the HSP rocks on Al_2O_3/SiO_2 versus MgO/SiO_2 diagram (Jagoutz *et al.* 1979; Hart & Zindler, 1986). The HSP rocks extend from peridotites in more fertile $Al_2O_3/SiO_2 = 0.07–0.09$ and $MgO/SiO_2 = 1.1–1.14$ and more refractory peridotites ($Al_2O_3/SiO_2 = 0.00–0.05$ and $MgO/SiO_2 = 0.75–1.1$); they all plot along or above the terrestrial array.

compositions compared to other domains. Figure 8d shows the relationship between the Nd isotopic compositions and $(Ce/Yb)_N$ ratios of the HSP rocks. In this diagram, the DP trend is characterized by higher εNd values (εNd > +10) and more depleted LREE patterns ($(Ce/Yb)_N$ <0.5) compared to the MORB source (εNd = +10 (White & Hofmann, 1982) and $(Ce/Yb)_N = 0.66$ (Sun & McDonough, 1989)). The HSP samples exhibit enriched REE signatures, and they plot in the EP field. The EP field is formed by mixing between an enriched component and residual peridotites (McCulloch & Chappel, 1982); only continental crustal material shows such enriched characteristics (i.e. fluids or melts derived from the continental crust have an average $(Ce/Yb)_N = 4$). Thus, the minor mantle metasomatism of the HSP rocks was derived from continental crustal materials associated with the subducted slab (Fig. 8b, c, d). Additionally, the calculated values of the Sm/Nd and Rb/Sr differentiation factors ($f_{(Sm/Nd)}$ and $f_{(Rb/Sr)}$ (McCulloch & Wasserburg, 1978)) are shown in Table 3. The careful use of these equations ($f_{(Sm/Nd)}$ and $f_{(Rb/Sr)}$ values) allows us to identify the mixing of a source with continental crustal material. The $f_{(Sm/Nd)}$ values range from –0.52 to 0.23, and the $f_{(Rb/Sr)}$ values range from –1 to 72, which confirms that the mantle source of the HSP rocks experienced the minor contribution of continental crustal materials associated with the subducting slab.

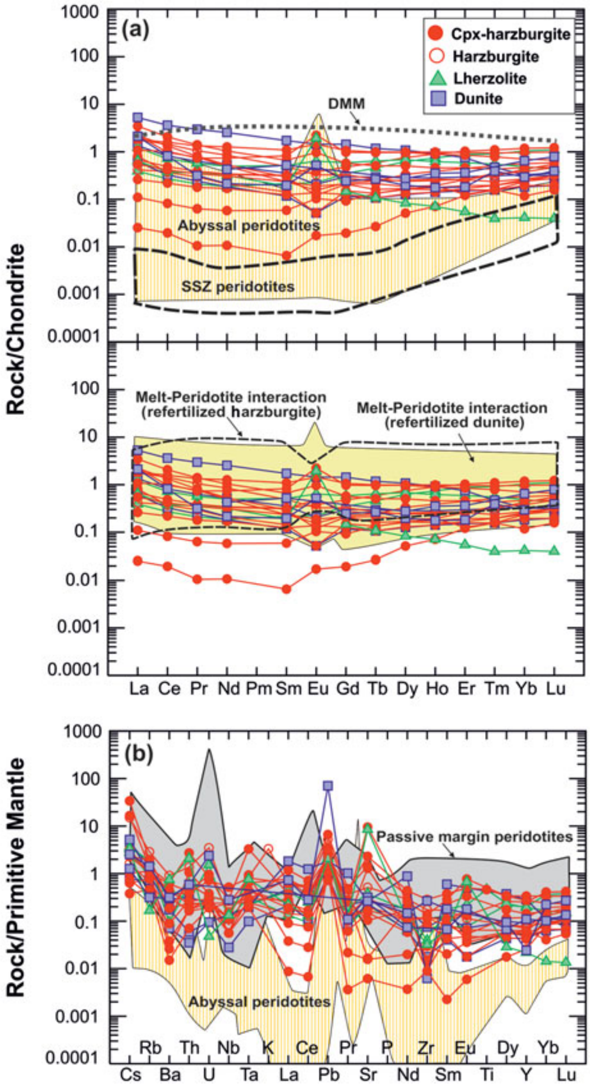

Figure 7. (Colour online) (a) Chondrite-normalized abundances of REE in the HSP rocks (Sun & McDonough, 1989). The supra-subduction zone (SSZ) peridotite field is from Parkinson & Pearce (1998). The DMM field is from Sun & McDonough (1989). Fields of abyssal peridotites and melt/rock interaction are from Deschamps *et al.* (2013). The solid line field (abyssal peridotites + melt/rock interactions) shows characteristics of refertilized protolith after melt/rock interactions. (b) Trace element abundances normalized by primitive mantle values (Sun & McDonough, 1989). The solid line field (abyssal peridotites + melt/rock interactions) shows characteristics of refertilized protolith after melt/rock interactions. The field of passive margin serpentinized peridotites is based on data from Newfoundland and the Iberian abyssal plain from Seifert & Brunotte (1996), Niu (2004), Savov *et al.* (2005, 2007), Deschamps *et al.* (2011, 2012) and Kodolányi *et al.* (2012).

8. Discussion

8.a. Evidence of melt depletion

The petrographic, major and trace element characteristics of the HSP rocks indicate that they represent the refractory and depleted mantle residues following partial melting. The geochemical and petrographical evidence includes: (1) the orthopyroxene grains with exsolution lamellae of clinopyroxene and spinel or between orthopyroxene and olivine (Fig. 4h, i), olivines with kink band features and partial replacement of orthopyroxene by olivine (Fig. 4b); (2) their low $^{143}Nd/^{144}Nd_{(i)}$ ratios (0.51208–0.51285); (3) the forsteritic composition of primary olivine (Fo: 91.1–94.9); (4) the depletion of the HSP samples in terms of their major oxide (Al_2O_3, TiO_2, CaO and MnO),

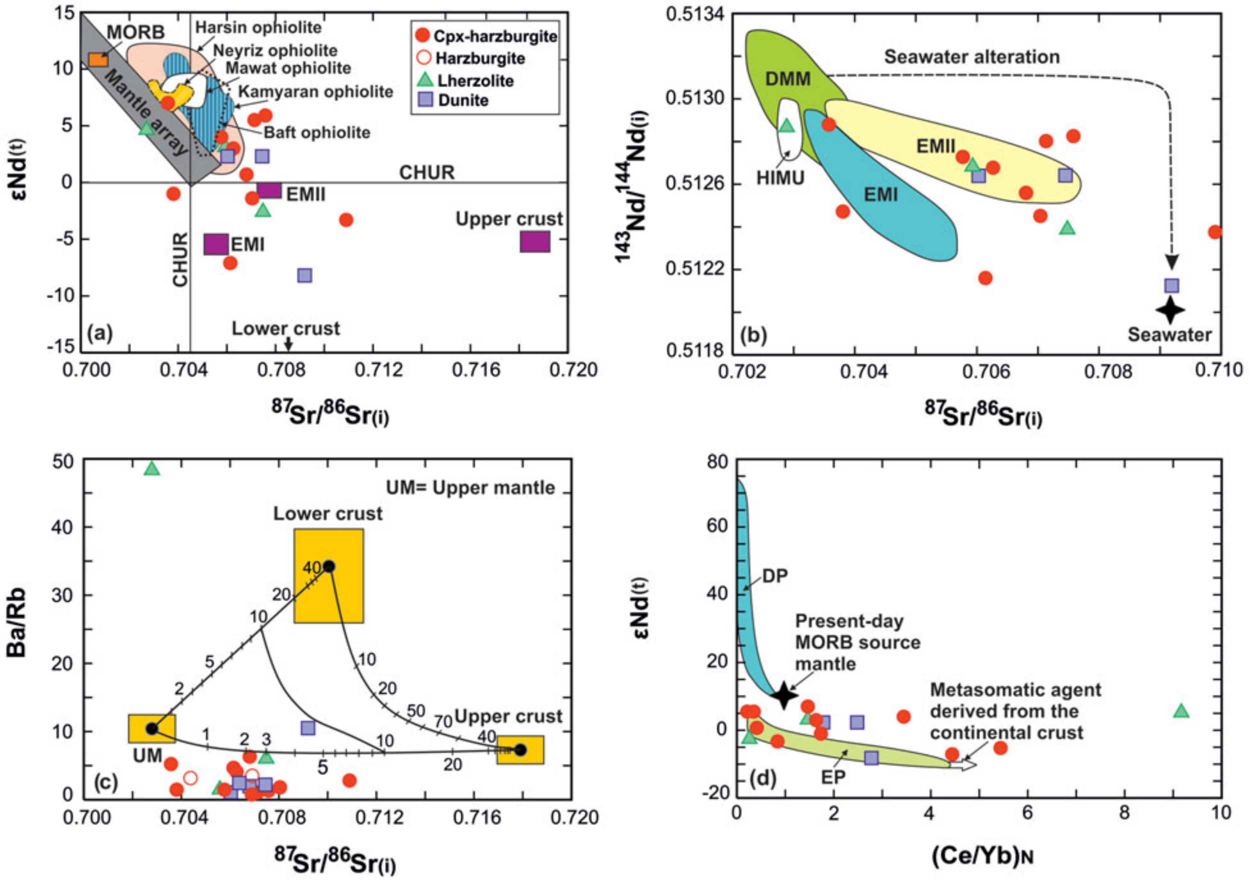

Figure 8. (Colour online) (a) The variations in $^{87}Sr/^{86}Sr_{(i)}$ versus $\varepsilon Nd_{(t)}$. The samples plot near the mantle array and extend from the field of the depleted mantle toward the fields of the EMII end-member component and seawater component. (b) The variations in $^{87}Sr/^{86}Sr_{(i)}$ versus $^{143}Nd/^{144}Nd_{(i)}$. The field of mantle components is based on data compiled by Stracke, Bizimis & Salters, (2003) for Atlantic MORB (DMM). Saint Helena (HIMU), Samoa and Society (EMII) and Pitcairn (EMI). The samples extend toward the EMII end-member, suggesting a minor contribution from EMII to the depleted mantle in their sources. The Sr and Nd isotopic compositions of seawater are from the literature: Palmer & Edmond (1989) for Sr and Nd compositions and Piepgras & Wasserburg (1987) and Tachikawa, Jeandel & Roy Barman, (1999) for Nd isotopic compositions. The fields of the Eocene Kamyaran ophiolite and Late Cretaceous Mawat ophiolite are from Azizi *et al.* (2011b) and Azizi *et al.* (2013), the data for the Late Cretaceous Neyriz ophiolite are from Shafaii Moghadam *et al.* (2014), the data for the Late Cretaceous Balvard–Baft ophiolite are from Shafaii Moghadam *et al.* (2013), and the data for the Harsin ophiolite are from Nouri (2016). (c) Sr isotope versus Ba/Rb diagram showing mixing between upper/lower crust and upper mantle peridotites. The Ba/Rb ratio of the lower crust is based on mafic granulites from the Dabie orogeny in Hou (2003). The Ba and Rb data for the UM and upper crust are from Sun & McDonough (1989). The Sr–Nd data for UM (upper mantle peridotite) are from Jahn *et al.* (1999), and the Sr–Nd data for the lower and upper crust are from Xu *et al.* (2004) and Jahn *et al.* (1999). (d) $(Ce/Yb)_N$ versus εNd. Star indicates the $(Ce/Yb)_N$ and εNd compositions of the present-day MORB (White & Hofmann, 1982; Sun & McDonough, 1989).

incompatible trace element (V, Sc, Y, Zn) and HREE contents; and (5) their variously depleted REE patterns compared to the depleted mantle on chondrite- and primitive mantle-normalized diagrams. Additionally, their observed whole-rock geochemical compositions are consistent with those of refractory and depleted mantle residues, which can also be seen on the MgO/SiO_2 versus Al_2O_3/SiO_2 diagram, where these samples lie on the depleted end of the terrestrial melting trend (Fig. 6). On the TiO_2 versus Cr_2O_3 diagram (Fig. 5a), the spinel compositions of the HSP rocks fall within the field of depleted oceanic peridotites (tectonites). This can also be seen on the TiO_2 versus Cr# diagram for spinel (Fig. 9), where the HSP spinels fall within the field of refractory abyssal peridotites defined by Kelemen *et al.* (1997) and Suhr *et al.* (2003); additionally, indicating that they represent mantle residues.

8.b. Water–rock interaction or melt refertilization?

The chemical compositions of the HSP rocks exhibit similar properties to refractory peridotites. Generally, the refractory peridotites are residues of high degrees of partial melting; their whole-rock REE patterns should be characterized by strong LREE depletion and flat to enriched MREE–HREE contents (Johnson, Dick & Shimizu, 1990; Johnson & Dick, 1992). Nevertheless, the bulk compositions of the HSP rocks exhibit different patterns, with light rare earth elements (LREE) and large-ion lithophile elements (LILE) enrichment (Fig. 7). Therefore, there must be another

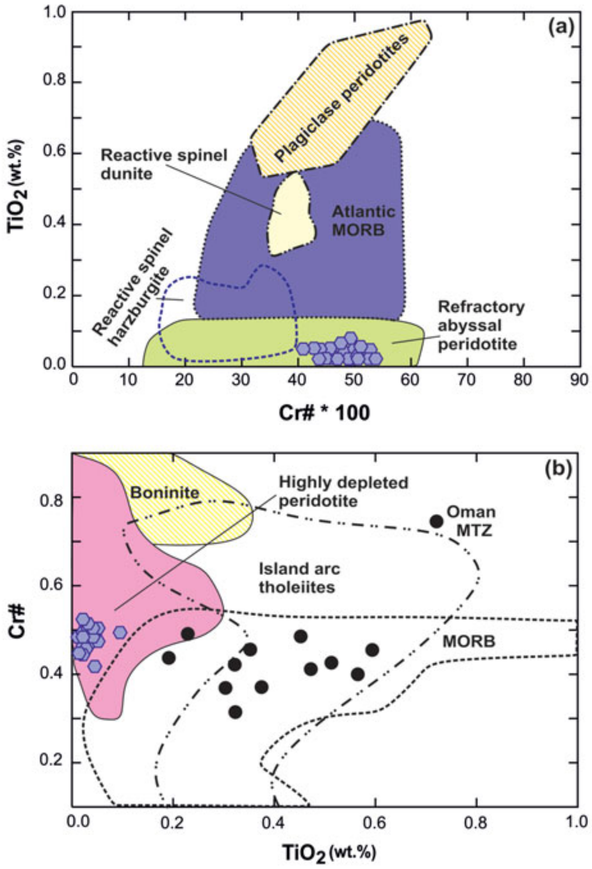

Figure 9. (Colour online) (a) TiO_2 versus Cr# diagram for the HSP spinels. The spinel samples fall within the field of refractory abyssal peridotite. The fields of refractory abyssal peridotites and Atlantic MORB are after Kelemen *et al.* (1997). (b) TiO_2 versus Cr# of spinels, the area for highly depleted peridotite from the Bay of Island ophiolite (Suhr *et al.* 2003), Josephine ophiolite (Morgan, Liang & Kelemen, 2008) and Iwanaidake peridotite (Kubo, 2002). MORB, island arc and boninite fields from Arai (1992), Kelemen, Shimizu & Salters (1995) and Dick & Natland (1996). Small black circles: dunites and impregnated peridotites from the Moho transition zone (MTZ) of the Oman ophiolite (Koga, Kelemen & Shimizu, 2001).

process, such as water–rock interaction (Paulick *et al.* 2006; Delacour *et al.* 2008; Chen *et al.* 2013) or melt refertilization (Niu, 1997, 2004; Kelemen, Kikawa & Miller, 2007; Chen *et al.* 2013), that can explain the LREE and LILE enrichments in the HSP rocks; these are discussed below.

8.b.1. Water–rock interaction ratios

In many studies, Sr isotopes have been demonstrated to be an important geochemical tool in the determination of fluid–rock interactions (Hart, Erlank & Kable, 1974; Jacobsen & Wasserburg, 1979; Hess, Bender & Schilling, 1991; Kempton, Hawkesworth & Fowler, 1991; Gillis, Coogan & Pedersen, 2005). A significant shift in Sr isotope compositions provides a constraint on the degree of seawater–rock interaction and fluid fluxes during the formation and alteration of these rocks. Therefore, when considering the interactions between fluids derived from seawater and the oceanic lithosphere, the $^{87}Sr/^{86}Sr$ ratio is an effective parameter for assessing water–rock (W/R) ratios (Hart, Erlank & Kable, 1974; Hess, Bender & Schilling, 1991; Kempton & Hunter, 1997; Delacour *et al.* 2008) and reflecting the extent of seawater–rock interaction in the oceanic lithosphere. It is necessary to calculate W/R ratios to determine the effect of hydrothermal alteration on the REE patterns of the HSP samples and to provide evidence for the circulation of seawater into the oceanic crust (Paulick *et al.* 2006; Delacour *et al.* 2008; Chen *et al.* 2013):

$$W/R_{\mathrm{closedsystem}} = [(\varepsilon_r{}^i - \varepsilon_r{}^f)/\left(\varepsilon_r{}^f - \varepsilon_w{}^i\right)] \times (X_r/X_w) \quad (1)$$

$$W/R_{\mathrm{opensystem}} = (X_r/X_w) \times \ln[(\varepsilon_r{}^i - \varepsilon_r{}^f)/\left(\varepsilon_r{}^f - \varepsilon_w{}^i\right) + 1] \quad (2)$$

In this equation, W is the mass of the hydrothermal fluid, R is the mass of the rock being altered by the fluid, $\varepsilon_r{}^i$ is the initial isotopic ratio of the rock (i.e. 0.702689 for mantle peridotite) (Workman & Hart, 2005), $\varepsilon_r{}^f$ is the final isotopic ratio of the hydrothermally altered rock (Table 3), $\varepsilon_w{}^i$ is the initial isotopic composition of hydrothermal fluid (seawater) (i.e. 0.70916) (Palmer & Edmond, 1989), X_r is the elemental composition of the mantle peridotite (i.e. 6.1 ppm) (Workman & Hart, 2005) and X_w is the elemental composition of the hydrothermal fluid (i.e. 8 ppm) (Palmer & Edmond, 1989).

When the water–rock ratio is greater than 100, incompatible elements become mobile and reflect the composition of the fluid phase rather than that of the parent rock (Bau, 1991; Gillis, Ludden & Smith, 1992; Delacour *et al.* 2008; Li *et al.* 2010). The *W*/*R* ratios of the HSP samples in both closed and open systems (Table 3) are low, ranging from 0.02 to 6.98 for closed systems and from 0.11 to 1.77 for open systems (Table 3). These data confirm that the minor circulation of seawater occurred along deep faults and fractures in an extensional basin. The *W*/*R* ratios of these rocks indicate that most REEs were unaffected by the hydrothermal alteration described in Section 7.

8.b.2. Melt refertilization

Melt refertilization is a common process in peridotites that has been studied in marine samples and ophiolitic successions (Godard, Bodinier & Vasseur, 1995; Seyler & Bonatti, 1997; Piccardo *et al.* 2003; Augustin *et al.* 2012). Trace element data from the serpentinized peridotites indicate that the geochemical characteristics of melt refertilization can even be preserved in altered ultramafic rocks (Paulick *et al.* 2006; Augustin *et al.* 2012; Chen *et al.* 2013; Manuella *et al.* 2016). The geochemical features related to melt refertilization include concordant increases in the concentrations of REEs and high field strength elements in bulk-rock peridotite samples (Niu, 2004; Augustin *et al.* 2012; Chen *et al.* 2013). This is due to the fact that REEs and HFSEs have similar solubilities in mafic melts, and this signature is transferred to peridotite. The trace element compositions of the serpentinized HSP rocks show positive trends on the Ce versus Th and La versus Nb diagrams (Fig, 10a, b), which indicates that melt–rock interaction is the dominant factor controlling these compositional variations, although some samples record evidence of minor fluid–rock interactions. These samples follow the trend of the global dataset, in which melt–rock interaction is the dominant process. This relationship indicates that the variability in LREEs is due to melt–rock interaction with minor hydrothermal alteration, which affects some HFSEs. Moreover, the geochemical characteristics of the HSP rocks in the Th versus Gd/Lu diagram display a similar trend of melt–rock interaction and exhibit enrichments in LREEs and HFSEs (Fig. 10c). In addition, these enrichments are confirmed by the La/Sm versus Sm/Yb diagram, which indicates that these samples have similar properties to the refertilized portion and exhibit enrichments in LREEs (Fig. 10d). Although Pb was previously considered to be a highly mobile element during hydrothermal alteration and dehydration in subduction zones (Niu & OʼHara, 2003), recent studies by Niu (2004) and Godard *et al.* (2008) of altered abyssal peridotites demonstrated that the geochemical behaviour of Pb during alteration and weathering was consistent with that of highly incompatible elements. Thus, the variations in the Nb versus Pb contents (Fig. 10e) are indicative of melt/fluid – rock interaction. In this diagram (Fig. 10e), the samples record evidence of melt refertilization; this trend is magmatic and indicates that the positive correlation of Nb and Pb is due to melt refertilization (Niu, 2004; Paulick *et al.* 2006). The scatter of some HSP samples on the Nb versus Pb diagram appears to be due to hydrothermal alteration modifying the Pb concentrations (Fig. 10e).

Moreover, most of the HSP rocks have similar contents of REE and incompatible elements to refertilized abyssal serpentinized peridotites (melt–rock interaction (Fig. 7)). They are enriched in LILEs and LREEs and show a decoupling between Nb and Ta, with more enrichment in Ta. In Figure 11, the REE in the HSP rocks have similar patterns to abyssal serpentinized peridotites that underwent melt–rock (MRI) and fluid-rock (FRI) interactions; however, they do not have similar patterns to the average hydrothermal sediments from the Mid-Atlantic Ridge (MAR) (Dias & Barriga, 2006). These processes are supported by the significant correlation between LREEs and HFSEs (Fig. 10), which reflects melt refertilization with minor fluid–rock interaction. Furthermore, the REE patterns of the HSP rocks on the chondrite-normalized diagram (Sun & McDonough, 1989) are almost flat and did not experience seawater alteration, as they exhibit negative Ce anomaly (Fig. 11). Therefore, we conclude that the enrichments in LREEs and other trace elements are clear evidence of melt–rock interaction (i.e. positive correlations between some LREEs and HFSEs), with some samples recording evidence of minor fluid–peridotite interaction.

8.c. Textures produced by melting and melt refertilization

Based on the above discussions, the textures and geochemistry of the HSP rocks offer evidences of cooling and decompression, partial melting and melt–rock reactions; although each process produces a specific mineral texture, some textures are not limited to a specific process and instead reveal the collective effect of several processes. They typically consist of orthopyroxene grains with exsolution lamellae of clinopyroxene (Fig. 4c) and spinel, vermicular spinel located within orthopyroxene grains or between orthopyroxene and olivine porphyroclasts (Fig. 4h, i), and embayed and flame-like spinel grains (Fig. 4d, i) that are produced during cooling and decompression or by the partial melting of abyssal peridotites at low pressures (Edwards & Malpas, 1996; Pearce *et al.* 2000; Miller *et al.* 2003; Liu *et al.* 2010; Li *et al.* 2015). They are typical of oceanic mantle tectonites (Pearce *et al.* 2000; Tamura *et al.* 2008). Moseley (1984) and Tamura & Arai (2005) demonstrated that these types of cooling textures are widespread in both abyssal and SSZ peridotites, and are caused by a decrease in solubility of clinopyroxene and spinel in orthopyroxene due to cooling and decompression. In this stage, the partial melting of orthopyroxene leads to spinel/clinopyroxene intergrowths and the erosion of pyroxene grains (Fig. 4c) (Pearce *et al.* 2000; Miller *et al.* 2003; Liu *et al.* 2010). As partial melting continues and more melt is produced, vermicular, chain and flame-like spinel grains (Fig. 4h, i) are formed within orthopyroxene or olivine crystals. Moreover, high degrees of partial melting and melt–rock reactions can cause the breakdown of pyroxene and its pseudomorphic replacement of spinel. These evidences are widely observed in many peridotites and are related to cooling and decompression of mantle peridotites; they were produced by partial melting of primary or evolved mantle or melt–rock interaction (Siena & Coltorti, 1993; Edwards & Malpas, 1996; Roeder, Poustovetov & Oskarsson, 2001; Li *et al.* 2015).

Additionally, the vermicular grains of spinel located along grain boundaries and the interstitial clinopyroxene grains located between grains of olivine and orthopyroxene (Fig. 3f, g) are interpreted to represent the crystallization products of metasomatic melts (Morishita *et al.* 2007) and are also attributed to melt–rock interaction with incompletely extracted melts in abyssal peridotites (Seyler *et al.*, 2001, 2007; Morishita *et al.* 2007). New interstitial clinopyroxene grains indicate that the penetration of melt can cause reactions with rock (Pearce *et al.* 2000; Tamura *et al.*

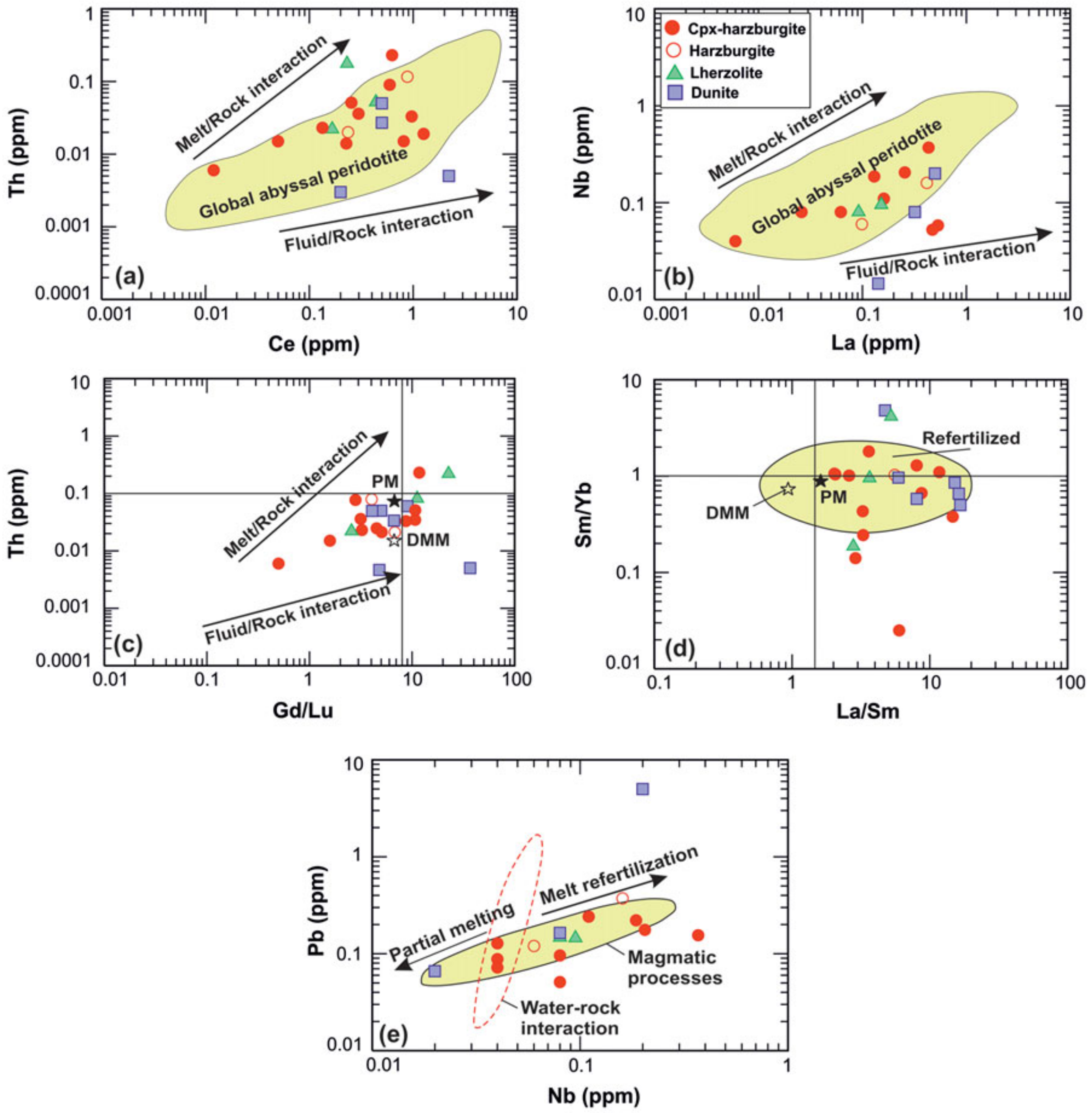

Figure 10. (Colour online) (a) Th versus Ce and (b) La versus Nb diagrams. Global abyssal peridotite field is from Niu (2004). (c) Th versus Gd/Lu ratio. Most of the samples show similar trends of melt/rock interaction. (d) Sm/Yb versus La/Sm diagram for the HSP rocks. The yellow field shows serpentinized peridotites from refertilized protoliths (Deschamps *et al.* 2013). (e) Nb versus Pb diagram. Most of the samples show trends of magmatic processes. The fields of partial melting, melt refertilization, water–rock interaction and magmatic processes are from Chen *et al.* (2013).

2008). Based on these textural and compositional data, we suggest that the HSP rocks are related by an increasing degree of depletion due to both partial melting and melt–rock reactions.

8.d. Trace element modelling of melting

We constrain the depleted nature of the HSP rocks based on evidence from geochemical data indicating that they represent mantle residues produced by various degrees and multiple episodes of partial melting. Mysen & Kushiro (1977) argued that if the mantle undergoes 2 % partial melting, its Cr# value will be 0.2, whereas with 10 % partial melting, its Cr# value will reach more than 0.3. If the Cr# of spinel reaches 0.22, the host rock underwent 10 % partial melting, whereas if the Cr# value reaches 0.5, the host rock underwent 15 % partial melting in the spinel lherzolite facies (Jaques & Green, 1980). Based on this idea, the Cr# values of the HSP rocks range from 0.41 to 0.52, which is consistent with 15−20 % partial melting of fertile spinel lherzolite. In addition, the abundances of Ni and Yb are less sensitive to melt–rock interaction or mantle metasomatism (Parkinson & Pearce, 1998; Green *et al.* 2000; Deschamps *et al.* 2010; Uysal *et al.* 2012) and are useful tools for estimating the degree of partial melting (Uysal *et al.* 2012; Kapsiotis, 2014). On the Yb versus Ni/Yb diagram, the HSP rocks are closely related to the residue produced by the 12–25 % partial melting of the primitive mantle (Fig. 12a). Chondrite-normalized REE patterns and curve calculated for non-modal fractional

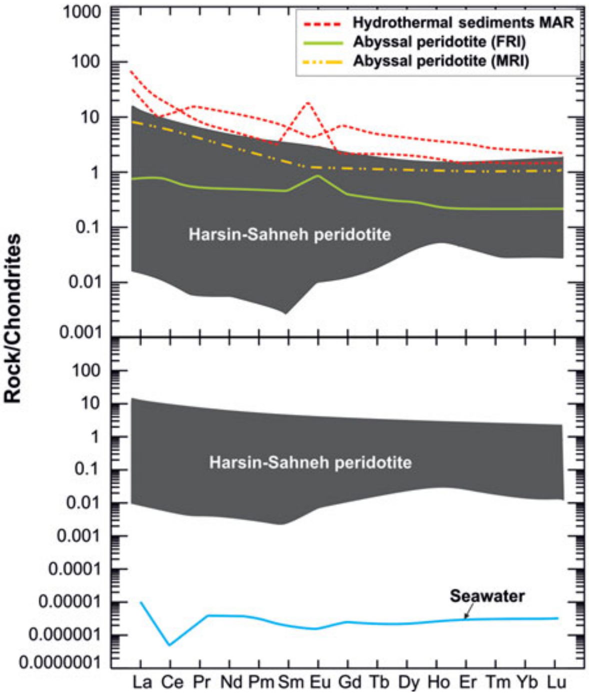

Figure 11. (Colour online) Chondrite-normalized REE abundances in the HSP rocks (Sun & McDonough, 1989). The hydrothermal sediment data from the MAR (Rainbow and Saldanha serpentinite host vent) are from Dias & Barriga (2006); data for abyssal peridotites that interacted with melt (MRI) and fluids (FRI) are from Paulick *et al.* (2006); and seawater data are from Turekian (1968).

melting of depleted MORB mantle (DMM) are shown in Figure 12b; in this diagram the HREEs variation coincides with the pattern calculated for 10–25 % melt extraction (Fig. 12b), because HREEs are less mobile than LREEs during mantle metasomatism (Aldanmaz *et al.* 2009; Niu *et al.* 2015; Marchesi *et al.* 2016). The LREE abundances are significantly different from the melting model estimation and are higher than the calculated LREE contents, indicating that these mantle rocks were enriched in LREEs during the syn- and/or post-melting interaction with fluid/melts (Aldanmaz *et al.* 2009; Marchesi *et al.* 2009, 2016; Niu *et al.* 2015).

8.d. Geodynamic implications and synthesis

The Harsin–Sahneh ophiolite complex, which is Jurassic to Late Cretaceous in age, has been interpreted as a suture zone between the Arabian and Iranian Plates. Previous data (Delaloye & Desmons, 1980; Desmons & Beccaluva, 1983; Ghazi & Hassanipak, 1999; Allahyari *et al.* 2010; Saccani *et al.* 2013) have suggested that the Harsin–Sahneh ophiolite formed at a mid-ocean ridge or island arc basin, whereas others (Wrobel Daveau *et al.* 2010; Azizi *et al.* 2013; Saccani *et al.* 2013; Nouri *et al.* 2016, 2017) have proposed that this zone formed in an undeveloped oceanic basin that was affected by a mantle plume.

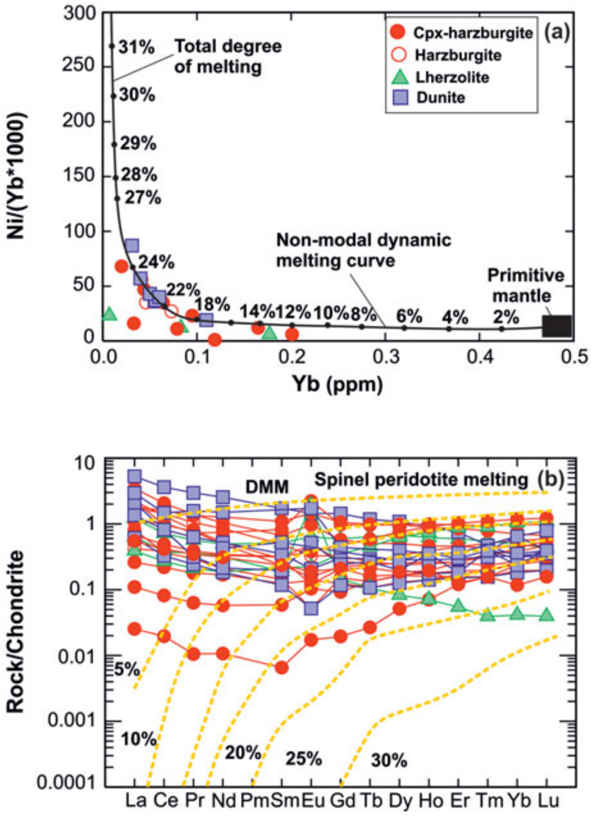

Figure 12. (Colour online) (a) Yb versus Ni/Yb diagram for the HSP rocks. The closed system non-modal dynamic melting model of primitive mantle with spinel-facies mantle mineralogy $Ol_{0.53(0.06)} + Opx_{0.27(0.67)} + Sp_{0.03(0.11)}$ is from Palme & O'Neill (2004) and Kinzler (1997). Partition coefficients are compiled from Suhr (1999), Green *et al.* (2000) and Adam & Green (2006). (b) Chondrite-normalized REE patterns for the HSP rocks. The samples are compared to the REE patterns calculated for anhydrous non-modal fractional melting of depleted mantle (DMM) (Salters & Stracke, 2004) in the spinel lherzolite facies (yellow dashed lines). Source and melting for olivine, orthopyroxene and clinopyroxene modal proportion are 0.54:0.28:0.18 and 0.11:0.59:0.53 at 1.5 GPa (Niu, 1997). Labels indicate partial melting degree. Partition coefficients are from Bedini & Bodinier (1999), Donnelly *et al.* (2004) and Su & Langmuir (2003). Normalizing values are from Sun & McDonough (1989).

As discussed above, our study shows that the HSP rocks have geochemical affinities to both MORB and supra-subduction-type rocks. These geochemical characteristics are directly related to a back-arc tectonic setting, which is supported by the elemental and isotopic signatures of the HSP rocks. We concluded that the evolution of the HSP rocks involved multiple episodes of depletion and refertilization. The less depleted HSP rocks may represent the restites produced by low degrees of partial melting during the first stage of partial melting in an extensional spreading basin. The trace element compositions of the less depleted HSP samples can be modelled by the low to moderate partial melting of a mantle source followed by interactions between the residual and percolating melt. In contrast, the highly depleted HSP rocks formed during the second stage of partial melting, followed by melt–peridotite interactions with the previously depleted mantle in an SSZ setting. The trace element abundances of the highly depleted peridotite can be explained by the high degree of partial melting of an already depleted mantle; this stage requires plate convergence and subduction, where the fluxing of the mantle by subduction melts caused the further melting of depleted peridotites to produce highly refractory residual compositions. These melting events are related to the drifting of the Arabian Plate during the Late Triassic – Early Jurassic (Delaloye & Desmons, 1980; Desmons & Beccaluva, 1983; Ghazi & Hassanipak, 1999; Dilek & Ahmed, 2003; Alavi, 2004; Jassim & Goff, 2006; Allahyari *et al.* 2010; Azizi *et al.* 2013; Saccani *et al.* 2013; Shafaii Moghadam & Stern, 2015; Nouri *et al.* 2016, 2017), such as the Neo-Tethys Ocean. During this stage, large volumes of HSP rocks were produced in an extensional spreading basin, as confirmed by the presence of some HSP rocks with a less depleted mantle origin. During this process, the HSP rocks were locally altered by seawater along deep faults and fractures. Then the initiation of subduction occurred from the Early Jurassic to the Late Cretaceous (Braud, 1978; Shahidi & Nazari, 1997; Azizi *et al.* 2013; Ao *et al.* 2016; Davoudian *et al.* 2016; Nouri *et al.* 2016), and they experienced a second melting episode, in which the less enriched component was derived from continental crustal materials associated with the subducted slab.

9. Conclusions

The high LREE contents and significantly positive correlations between LREEs and HFSEs in the HSP rocks reflect the refertilization of residual peridotites by porous melt flow. Their Sr isotopic ratios show that water–rock interactions may not have played an important role in enriching their LREE contents. In contrast, melt–rock interaction can be considered to be a main cause of the LREEs enrichment of these rocks. Based on our findings in this research, the HSP rocks were predominantly formed by the extraction of MORB-like magma from mantle peridotite at a mid-oceanic ridge or in a back-arc basin due to a combination of melt/rock interactions and a high degree of partial melting in a supra-subduction zone from the Late Triassic to Late Cretaceous.

Acknowledgements. This research is supported by a JSPS KAKENHI grant in Japan (no. 25303029). We would like to thank Nagoya University (Japan) for supporting F. Nouri in summer 2016 and the University of Kurdistan for supporting field trips. The authors would like to give special thanks to Prof. K. Yamamoto from Nagoya University for supporting our XRF and ICP-MS analyses. We are grateful to Prof. S. Wallis from Nagoya University for supporting EMP analyses and to K. Mano from Nagoya University for his technical assistance. This paper benefited greatly from critical comments by Dr C. Deering, Editor, and two anonymous reviewers.

References

Adam, J. & Green, T. 2006. Trace element partitioning between mica and amphibole bearing garnet harzburgite and hydrous basanitic melt: 1. Experimental results and the investigation of controls on partitioning behavior. *Contributions to Mineralogy and Petrology* **152**, 1–17.

Agard, P., Omrani, J., Jolivet, L. & Mouthereau, F. 2005. Convergence history across Zagros (Iran): constraints from collisional and earlier deformation. *International Journal of Earth Sciences* **94**, 401–19.

Aghazadeh, M., Castro, A., Rashidnejad Omran, N., Emami, M. H., Moinevaziri, H. & Badrzadeh, Z. 2010. The gabbro (shoshonitic) monzonite granodiorite association of Khankandi pluton, Alborz Mountains, NW Iran. *Journal of Asian Earth Sciences* **38**, 199–219.

Ahmed, A. H. & Habtoor, A. 2015. Heterogeneously depleted Precambrian lithosphere deduced from mantle peridotites and associated chromitite deposits of Al'Ays ophiolite, Northwestern Arabian Shield, Saudi Arabia. *Ore Geology Reviews* **67**, 279–96.

Alard, O., Luguet, A., Pearson, N. J., Griffin, W. L., Lorand, J. P., Gannoun, A., Burton, K. W. & O'Reilly, S. Y. 2005. In situ Os isotopes in abyssal peridotites bridge the isotopic gap between MORBs and their source mantle. *Nature* **436**, 1005–8.

Alavi, M. 2004. Regional stratigraphy of the Zagros fold-thrust belt of Iran and its proforeland evolution. *American Journal of Science* **304**, 1–20.

Aldanmaz, E., Schmidt, M. W., Gourgaud, A. & Meisel, T. 2009. Mid-ocean ridge and supra-subduction geochemical signatures in spinel–peridotites from the Neotethyan ophiolites in SW Turkey: implications for upper mantle melting processes. *Lithos* **113**, 691–708.

Allahyari, K., Pourmoafi, M. & Khalatbari-Jafari, M. 2012. Petrology and geochemistry of the extrusive sequence of Harsin ophiolite, W Iran. *Geoscience Scientific Quarterly Journal* **84**, 189—98 (in Persian).

Allahyari, K., Saccani, E., Pourmoafi, M., Beccaluva, L. & Masoudi, F. 2010. Petrology of mantle peridotites and intrusive mafic rocks from the Kermanshah ophiolitic complex (Zagros belt, Iran): implications for the geodynamic evolution of the Neo-Tethyan oceanic branch between Arabia and Iran. *Ofioliti* **35**, 71–90.

Allahyari, K., Saccani, E., Rahimzadeh, B. & Zeda, O. 2014. Mineral chemistry and petrology of highly magnessian ultramfic cumulates from the Sarve-Abad (Sawlava) ophiolites (Kurdistan, NW Iran): new evidence for boninitic magmatism in intra-oceanic fore-arc setting in the Neo-Tethys between Arabia and Iran. *Journal of Asian Earth Sciences* **79**, 312–28.

Allen, D. E. & Seyfried, W. E. 2005. REE controls in ultramafic hosted mid-ocean ridge hydrothermal systems: an experimental study at elevated temperature and pressure. *Geochimica Cosmochimica Acta* **69**, 675–83.

Ao, S., Xiao, W., Khalatbari-Jafari, M., Talebian, M., Chen, L., Wan, B. W. J. & Zhang, Z. 2016. U-Pb zircon ages, field geology and geochemistry of the Kermanshah ophiolite (Iran): from continental rifting at 79 Ma to oceanic core complex at ca. 36 Ma in the southern Neo-Tethys. *Gondwana Research* **31**, 305–18.

Arai, S. 1992. Chemistry of chromian spinel in volcanic rocks as a potential guide to magma chemistry. *Mineralogical Magazine* **56**, 173–84.

Arai, S. 1994. Characterization of spinel peridotites by olivine–spinel compositional relationships: review and interpretation. *Chemical Geology* **113**, 191–204.

Arai, S. & Yurimoto, H. 1994. Podiform chromitites of the Tari-Misaka ultramafic complex, southwestern Japan, as mantle-melt interaction products. *Economic Geology* **89**, 1279–88.

Augustin, N., Paulick, H., Lackschewitz, K. S., Eisenhauer, A., Garbe Schonberg, D., Kuhn, T., Botz, R. & Schmidt, M. 2012. Alteration at the ultramafic-hosted Logatchev hydrothermal field: constraints from trace element and Sr–O isotope data. *Geochemistry, Geophysics, Geosystems* **13**, Q0AE07. doi: 10.1029/2011GC003903.

Aziz, N. R., Elias, E. M. & Aswad, K. J. 2011. Rb–Sr and Sm–Nd isotope study of serpentinites and their impact on the tectonic setting of Zagros Suture Zone, NE-Iraq. *Iraqi Bulletin of Geology and Mining* **7**, 67–75.

Azizi, H., Asahara, Y., Mehrabi, B. & Chung, S. L. 2011a. Geochronological and geochemical constraints on the petrogenesis of high-K granite from the Suffi abad area, Sanandaj-Sirjan Zone, NW Iran. *Chemie der Erde / Geochemistry* **71**, 363–76.

Azizi, H., Hadi, A., Asahara, Y. & Mohammad, Y. O. 2013. Geochemistry and geodynamics of the Mawat mafic complex in the Zagros suture zone, northeast Iraq. *Central European Journal of Geosciences* **5**, 523–37.

Azizi, H., Kazemi, T. & Asahara, Y. 2017. A-type granitoid in Hasansalaran complex, northwestern Iran: evidence for extensional tectonic regime in northern Gondwana in the Late Paleozoic. *Journal of Geodynamics* **108**, 56–72.

Azizi, H., Najari, M., Asahara, Y., Catlos, E., Shimizu, M. & Yamamoto, K. 2015a. U–Pb zircon ages and geochemistry of Kangareh and Taghiabad mafic bodies in northern Sanandaj–Sirjan Zone, Iran: evidence for intra-oceanic arc and back-arc tectonic regime in Late Jurassic. *Tectonophysics* **660**, 47–64.

Azizi, H., Tanaka, T., Asahara, Y., Chung, S. L. & Zarrinkoub, M. H. 2011b. Discrimination of the age and tectonic setting for magmatic rocks along the Zagros thrust zone, northwest Iran, using the zircon U-Pb age and Sr-Nd isotopes. *Journal of Geodynamics* **52**, 304–20.

Azizi, H., Zanjefili Beiranvand, M. & Asahara, Y. 2015b. Zircon U–Pb ages and petrogenesis of a tonalite–trondhjemite–granodiorite (TTG) complex in the northern Sanandaj–Sirjan Zone, northwest Iran: evidence for Late Jurassic arc–continent collision. *Lithos* **216**, 178–95.

Baharifar, A., Moinevaziri, H., Bellon, H. & Pique, A. 2004. The crystalline complexes of Hamadan (Sanandaj–Sirjan zone, western Iran): metasedimentary Mesozoic sequences affected by Late Cretaceous tectono-metamorphic and plutonic events. *Comptes Rendus Geosciences* **336**, 1443–52.

Bau, M. 1991. Rare-earth element mobility during hydrothermal and metamorphic fluid-rock interaction and the significance of the oxidation stage of europium. *Chemical Geology* **93**, 219–30.

Bedini, R. M. & Bodinier, J. L. 1999. Distribution of incompatible trace elements between the constituents of spinel peridotite xenoliths: ICP-MS data from the East African Rift. *Geochimica et Cosmochimica Acta* **63**, 3883–900.

Berberian, M. & King, G. C. P. 1981. Towards a paleogeography and tectonic evolution of Iran. *Canadian Journal of Earth Science* **18**, 210–65.

Besse, J., Torcq, F., Gallet, Y., Ricou, L. E., Krystyn, L. & Saidi, A. 1998. Late Permian to Late Triassic palaeomagnetic data from Iran: constraints on the migration of the Iranian block through the Tethyan Ocean and initial destruction of Pangaea. *Geophysical Journal International* **135**, 77–92.

Braud, J. 1978. *Geology Map of Kermanshah, Scale 1:250000*. No. C6. Tehran: Geology Survey of Iran.

Chen, Z. Q., Zhou, H. Y., Liu, Y., Yang, Q. H., Li, J. W. & Dick, H. J. 2013. Influence of igneous processes and serpentinization on geochemistry of the Logatchev Massif harzburgites (14 45″ N, Mid-Atlantic Ridge), and comparison with global abyssal peridotites. *International Geology Review* **55**, 115–30.

Choi, S. H., Shervais, J. W. & Mukasa, S. B. 2008. Supra-subduction and abyssal mantle peridotites of the Coast Range ophiolite, California. *Contributions to Mineralogy and Petrology* **156**, 551–76.

Davoudian, A., Genser, J., Dachs, E. & Shabanian, N. 2008. Petrology of eclogites from north of Shahrekord, Sanandaj-Sirjan Zone, Iran. *Mineralogy and Petrology* **92**, 393–413.

Davoudian, A. R., Genser, J., Neubauer, F. & Shabanian, N. 2016. ^{40}Ar/^{39}Ar mineral ages of eclogites from North Shahrekord in the Sanandaj–Sirjan Zone, Iran: implications for the tectonic evolution of Zagros orogen. *Gondwana Research*, **37**, 216–40.

Davoudzadeh, M. & Schmidt, K. 1984. A review of the Mesozoic paleogeography and paleotectonic evolution of Iran. *Neues Jahrbuch für Geologie und Palaeontologie Abhandlungen* **168**, 182–207.

Deer, W., Howie, R. & Zussman, J. 1992. *An Introduction to the Rock Forming Minerals*. Harlow: Longman Scientific and Technical, 696 pp.

Delacour, A., Früh Green, G. L., Frank, M., Gutjahr, M. & Kelley, D. S. 2008. Sr and Nd-isotope geochemistry of the Atlantis Massif (30°N, MAR): implications for fluid fluxes and lithospheric heterogeneity. *Chemical Geology* **254**, 19–35.

Delaloye, M. & Desmons, J. 1980. Ophiolites and mélange terranes in Iran: a geochronological study and its paleotectonic implications. *Tectonophysics* **68**, 83–111.

DePaolo, D. J. & Wasserburg, G. J. 1976. Nd isotopic variations and petrogenetic models. *Geophysical Research Letters* **3**, 249–52.

Deschamps, F., Godard, M., Guillot, S., Chauvel, C., Andreani, M., Hattori, K., Wunder, B. & France, L. 2012. Behavior of fluid-mobile elements in serpentines from abyssal to subduction environments: examples from Cuba and Dominican Republic. *Chemical Geology* **312**, 93–117.

Deschamps, F., Godard, M., Guillot, S. & Hattori, K. 2013. Geochemistry of subduction zone serpentinites: a review. *Lithos* **178**, 96–127.

Deschamps, F., Guillot, S., Godard, M., Andreani, M. & Hattori, K. 2011. Serpentinites act as sponges for fluid-mobile elements in abyssal and subduction zone environments. *Terra Nova* **23**, 171–8.

Deschamps, F., Guillot, S., Godard, M., Chauvel, C., Andreani, M. & Hattori, K. 2010. In situ characterization of serpentinites from forearc mantle wedges: timing of serpentinization and behavior of fluid-mobile elements in subduction zones. *Chemical Geology* **269**, 262–77.

Desmons, J. & Beccaluva, L. 1983. Mid-oceanic ridge and island arc affinities in ophiolites from Iran: paleogeographic implication. *Chemical Geology* **39**, 39–63.

Dias, A. S. & Barriga, F. J. A. S. 2006. Mineralogy and geochemistry of hydrothermal sediments from the serpentinite-hosted Saldanha hydrothermal field (36° 34′ N; 33° 26′ W) at MAR. *Marine Geology* **225**, 157–75.

Dick, H. J. & Bullen, T. 1984. Chromian spinel as a petrogenetic indicator in abyssal and alpine type peridotites and spatially associated lavas. *Contributions to Mineralogy and Petrology* **86**, 54–76.

Dick, H. J. B. & Natland, J. H. 1996. Late-stage melt evolution and transport in the shallow mantle beneath the East Pacific Rise. *Proceedings of the Ocean Drilling Program, Scientific Results* **147**, 103–34.

Dilek, Y. & Ahmed, Z. 2003. Proterozoic ophiolites of the Arabian Shield and their significance in Precambrian tectonics. In *Ophiolites in Earth History* (eds Y. Dilek & P. T. Robinson), pp. 685–700. Geological Societyof London, Special Publication no. 218.

Dilek, Y., Furnes, H. & Shallo, M. 2007. Suprasubduction zone ophiolite formation along the periphery of Mesozoic Gondwana. *Gondwana Research* **11**, 453–75.

Donnelly, K. E., Goldstein, S. L., Langmuir, C. H. & Spiegelman, M. 2004. Origin of enriched ocean ridge basalts and implications for mantle dynamics. *Earth and Planetary Science Letters* **226**, 347–66.

Douville, E., Charlou, J. L., Oelkers, E. H., Bienvenu, P., Jove Colon, C. F., Donval, J. P., Fouquet, Y., Pricur, D. & Appriou, P. 2002. The Rainbow vent fluids (36° 14′ N, MAR): the influence of ultramafic rocks and phase separation on trace element content in mid-Atlantic ridge hydrothermal fluids. *Chemical Geology* **184**, 37–48.

Edwards, S. J. & Malpas, J. 1996. Melt-peridotite interactions in shallow mantle at the East Pacific Rise: evidence from ODP Site 895 (Hess Deep). *Mineralogical Magazine* **60**, 191–206.

Eshraghi, S. A., Jafarian, M. B. & Eshraghi, B. 1996. *Geological Map of Sonqor*. Quadrangle 5559. Tehran: Geological Survey of Iran.

Esmaeily, D., Nedelec, A., Valizadeh, M. V., Moore, F. & Cotton, J. 2005. Petrology of the Jurassic Shah-Kuh granite (eastern Iran), with reference to tin mineralization. *Journal of Asian Earth Sciences* **25**, 961–80.

Eyuboglu, Y., Santosh, M. & Chung, S. L. 2011. Crystal fractionation of adakitic magmas in the crust–mantle transition zone: petrology, geochemistry and U–Pb zircon chronology of the Seme adakites, Eastern Pontides, NE Turkey. *Lithos* **121**, 151–66.

Ghazi, A. M. & Hassanipak, A. A. 1999. Geochemistry of subalkaline and alkaline extrusive from of the Kermanshah ophiolite, Zagros Suture Zone, Western Iran: implications for Tethyan plate tectonics. *Journal of Asian Earth Sciences* **17**, 319–32.

Ghorbani, M. R. & Bezenjani, R. N. 2011. Slab partial melts from the metasomatizing agent to adakite, Tafresh Eocene volcanic rocks, Iran. *Island Arc* **20**, 188–202.

Ghorbani, M. R., Graham, I. T. & Ghaderi, M. 2014. Oligocene–Miocene geodynamic evolution of the central part of Urumieh-Dokhtar Arc of Iran. *International Geology Review* **56**, 1039–50.

Gillis, K. M., Coogan, L. A. & Pedersen, R. 2005. Strontium isotope constraints on fluid flow in the upper oceanic crust at the East Pacific Rise. *Earth and Planetary Science Letters* **232**, 83–94.

Gillis, K. M., Ludden, J. N. & Smith, A. D. 1992. Mobilization of the REE during crustal aging in the Troodos ophiolite, Cyprus. *Chemical Geology* **98**, 71–86.

Godard, M., Bodinier, J. L. & Vasseur, G. 1995. Effects of mineralogical reactions on trace element redistributions in mantle rocks during percolation processes: a chromatographic approach. *Earth and Planetary Science Letters* **133**, 449–61.

Godard, M., Lagabrielle, Y., Alard, O. & Harvey, J. 2008. Geochemistry of the highly depleted peridotites drilled at ODP Sites 1272 and 1274 (Fifteen–Twenty Fracture Zone, Mid-Atlantic Ridge): implications for mantle dynamics beneath a slow spreading ridge. *Earth and Planetary Science Letters* **267**, 410–25.

Green, T., Blundy, J. D., Adam, J. & Yaxley, G. M. 2000. SIMS determination of trace element partition coefficients between garnet, clinopyroxene and hydrous basaltic liquids at 2–7.5 GPa and 1080–1200°C. *Lithos* **53**, 165–87.

Hart, S. R., Erlank, A. J. & Kable, E. J. D. 1974. Sea floor basalt alteration: some chemical and Sr isotopic effects. *Contributions to Mineralogy and Petrology* **44**, 219–30.

Hart, S. R. & Zindler, A. 1986. In search of a bulk-earth composition. *Chemical Geology* **57**, 247–67.

Hawkins, J. W. & Allan, J. F. 1994. Petrologic evolution of Lau Basin sites 834 through 839. *Proceedings of the Ocean Drilling Program, Scientific Results* **135**, 427–70.

Herbert, R. 1982. Petrography and mineralogy of oceanic peridotites and gabbros: some comparisons with ophiolite examples. *Ofioliti* **7**, 299–324.

Hess, J., Bender, M. & Schilling, J. G. 1991. Assessing seawater/basalt exchange of strontium isotopes in hydrothermal processes on the flanks of mid-ocean ridges. *Earth and Planetary Science Letters* **103**, 133–42.

Hou, Z. H. 2003. *Zirconium geochemistry, trace elemental characters of zircons and its chronological applications of high-grade metamorphic rocks in the Dabie–Sulu orogen*. Ph.D. thesis, University of Science and Technology of China, Hefei, China. Published thesis.

Hout, F., Hébert, R., Varfalvy, V., Beaudoin, G., Wang, C. S., Liu, Z. F., Cotten, J. & Dostal, J. 2002. The Beimarang Melange (Southern Tibet) brings additional constraints in assessing the origin, metamorphic evolution and obduction processes of the Yarlung Zangbo Ophiolite. *Journal of Asian Earth Sciences* **21**, 307–22.

Jacobsen, S. B. & Wasserburg, G. J. 1979. Nd and Sr isotopic study of the Bay of Islands ophiolitic complex and the evolution of the source of the mid ocean ridge basalts. *Journal of Geophysical Research* **84**, 7429–45.

Jagoutz, E., Palme, H., Baddenhausen, H., Blum, K., Cendales, M., Dreibus, G., Spettel, B., Wänke, H. & Lorenz, V. 1979. The abundances of major, minor and trace elements in the earth's mantle as derived from primitive ultramafic nodules. *In Lunar and Planetary Science Conference Proceedings* **10**, 2031–50.

Jahn, B., Wu, F., Lo, C. H. & Tsai, C. H. 1999. Crust-mantle interaction induced by deep subduction of the continental crust: geochemical and Sr–Nd isotopic evidence from post-collisional mafic–ultramafic intrusions of the northern Dabie complex. *Chemical Geology* **157**, 119–46.

Jan, M. & Windley, B. 1990. Chromian spinel silicate chemistry in ultramafic rocks of the Jijal complex, northwest Pakistan. *Journal of Petrology* **31**, 667–715.

Jaques, A. L. & Green, D. H. 1980. Anhydrous melting of peridotite at 0–15 kb pressure and the genesis of tholeiitic basalts. *Contributions to Mineralogy and Petrology* **73**, 287–310.

Jassim, S. Z. & Goff, J. 2006. *Geology of Iraq*. Brno: Dolin, Prague and Moravian Museum, 337 pp.

Jean, M. M., Shervais, J. W., Choi, S. H. & Mukasa, S. B. 2010. Melt extraction and melt refertilization in mantle peridotite of the Coast Range ophiolite: an LA–ICP–MS study. *Contributions to Mineralogy and Petrology* **159**, 113–36.

Johnson, K. T. M. & Dick, H. J. B. 1992. Open system melting and temporal and spatial variation of peridotite and basalt at the Atlantis II fracture zone. *Journal of Geophysical Research* **97**, 9219–41.

Johnson, K. T. M., Dick, H. J. B. & Shimizu, N. 1990. Melting in the oceanic upper mantle: an ion microprobe study of diopsides in abyssal peridotites. *Journal of Geophysical Research* **95**, 2661–78.

Kapsiotis, A. N. 2014. Compositional signatures of SSZ-type peridotites from the northern Vourinos ultra-depleted upper mantle suite, NW Greece. *Chemie der Erde / Geochemistry* **74**, 783–801.

Karimi Bavandpur, A. & Hajihoseini, A. 1999. *Geological Map of Kermanshah*. Quadrangle 5458. Tehran: Geological Survey of Iran.

Karipi, S., Tsikouras, B. & Hatzipanagiotou, K. 2006. The petrogenesis and tectonic setting of ultramafic rocks from Iti and Kallidromon Mountains, continental Central Greece: vestiges of the Pindos Ocean. *Canadian Mineralogist* **44**, 267–87.

Kelemen, P. B., Hirth, G., Shimizu, N., Spiegelman, M. & Dick, H. J. B. 1997. A review of melt migration processes in the adiabatically upwelling mantle beneath oceanic spreading ridges. *Philosophical Transactions of the Royal Society of London, Series* **355**, 283–318.

Kelemen, P. B., Kikawa, E. & Miller, D. J. 2007. Leg 209 summary: Processes in a 20-km-thick conductive boundary layer beneath the Mid-Atlantic Ridge, 14°–16°N. *Proceedings of the Ocean Drilling Program, Scientific Results* **209**, 1–33.

Kelemen, P. B., Shimizu, N. & Salters, V. J. M. 1995. Extraction of mid-ocean-ridge basalt from the upwelling mantle by focused flow of melt in dunite channels. *Nature* **375**, 747–53.

Kempton, P. D., Hawkesworth, C. J. & Fowler, M., 1991. Geochemistry and isotopic composition of gabbros from layer 3 of the Indian Ocean crust, Hole 735B. *Proceedings of the Ocean Drilling Program, Scientific Results* **118**, 127–43.

Kempton, P. D. & Hunter, A.G. 1997. A Sr, Nd, Pb, O isotope study of plutonic rocks from MARK, leg 153: implications for mantle heterogeneity and magma *Proceedings of the Ocean Drilling Program, Scientific Results* **153**, 305–19.

Kinzler, R. J. 1997. Melting of mantle peridotite at pressures approaching the spinel to garnet transition: application to mid-ocean ridge basalt petrogenesis. *Journal of Geophysical Research* **102**, 853–74.

Klinkhammer, G. P., Elderfield, H., Edmond, J. M. & Mitra, A. 1994. Geochemical implications of rare earth element patterns in hydrothermal fluids from mid-ocean ridges. *Geochimica Cosmochimica Acta* **58**, 5105–113.

Kodolányi, J., Pettke, T., Spandler, C., Kamber, B. S. & Gméling, K. 2012. Geochemistry of ocean floor and fore-arc serpentinites: constraints on the ultramafic input to subduction zones. *Journal of Petrology* **53**, 235–70.

Koga, K. T., Kelemen, P. B. & Shimizu, N. 2001. Petrogenesis of the crust–mantle transition zone and the origin of lower crustal wehrlite in the Oman ophiolite. *Geochemistry, Geophysics, Geosystems* **2**. doi: 10.1029/2000GC000132.

Kubo, K. 2002. Dunite formation processes in highly depleted peridotite: case study of the Iwanaidake peridotite, Hokkaido, Japan. *Journal of Petrology* **43**, 423–48.

Li, X. P., Chen, H. K., Wang, Z. L., Wang, L. J., Yang, J. S. & Robinson, P. 2015. Spinel peridotite, olivine websterite and the textural evolution of the Purang ophiolite complex, western Tibet. *Journal of Asian Earth Sciences* **110**, 55–71.

Li, X. P., Zhang, L. F., Wilde, S. A., Song, B. & Liu, X. M. 2010. Zircons from rodingite in the Western Tianshan serpentinite complex: mineral chemistry and U–Pb ages define nature and timing of rodingitization. *Lithos* **118**, 17–34.

Liu, C. Z., Wu, F. Y., Wilde, S. A., Yu, L. J. & Li, J. L. 2010. Anorthitic plagioclase and pargasitic amphibole in mantle peridotites from the Yungbwa ophiolite (southwestern Tibetan Plateau) formed by hydrous melt metasomatism. *Lithos* **114**, 413–22.

Luguet, A., Alard, O., Lorand, J. P., Pearson, N. J., Ryan, C. & O'Reilly, S. Y. 2001. Laser ablation microprobe (LAM)-ICPMS unravels the highly siderophile element geochemistry of the oceanic mantle. *Earth and Planetary Science Letters* **189**, 285–94.

Mahmoudi, S., Corfu, F., Masoudi, F., Mehrabi, B. & Mohajjel, M. 2011. U–Pb dating and emplacement history of granitoid plutons in the northern Sanandaj–Sirjan Zone, Iran. *Journal of Asian Earth Sciences* **41**, 238–49.

Manuella, F. C., Ottolini, L., Carbone, S. & Scavo, L. 2016. Metasomatizing effects of serpentinization-related hydrothermal fluids in abyssal peridotites: new contributions from Hyblean peridotite xenoliths (southeastern Sicily). *Lithos* **264**, 405–21.

Marchesi, C., Garrido, C. J., Bosch, D., Bodinier, J. L., Gervilla, F. & Hidas, K. 2013. Mantle refertilization by melts of crustal-derived garnet pyroxenite: evidence from the Ronda peridotite massif, southern Spain. *Earth and Planetary Science Letters* **362**, 66–75.

Marchesi, C., Garrido, C. J., Godard, M., Belley, F. & Ferré, E. 2009. Migration and accumulation of ultra-depleted subduction-related melts in the Massif du Sud ophiolite (New Caledonia). *Chemical Geology* **266**, 171–86.

Marchesi, C., Garrido, C. J., Godard, M., Proenza, J. A., Gervilla, F. & Blanco-Moreno, J. 2006. Petrogenesis of highly depleted peridotites and gabbroic rocks from the Mayarí-Baracoa Ophiolitic Belt (eastern Cuba). *Contributions to Mineralogy and Petrology* **151**, 717–36.

Marchesi, C., Garrido, C. J., Proenza, J. A., Hidas, K., Varas-Reus, M. I., Butjosa, L. & Lewis, J. F. 2016. Geochemical record of subduction initiation in the sub-arc mantle: insights from the Loma Caribe peridotite (Dominican Republic). *Lithos* **252–253**, 1–15.

Marchesi, C., Jolly, W. T., Lewis, J. F., Garrido, C. J., Proenza, J. A. & Lidiak, E. G. 2011. Petrogenesis of fertile mantle peridotites from the Monte del Estado massif (Southwest Puerto Rico): a preserved section of Proto-Caribbean lithospheric mantle? *Geologica Acta* **9**, 289–306.

McCulloch, M. T. & Chappel, B. W. 1982. Nd isotopic characteristics of S- and I-type granites. *Earth and Planetary Science Letters* **58**, 51–64.

McCulloch, M. T. & Wasserburg, G. J. 1978. Barium and neodymium isotopic anomalies in the Allende meteorite. *Astrophysical Journal* **220**, 15–19.

Melcher, F., Meisel, T., Puhl, J. & Koller, F. 2002. Petrogenesis and geotectonic setting of ultramafic rocks in the Eastern Alps: constraints from geochemistry. *Lithos* **65**, 69–112.

Miller, C., Thöni, M., Frank, W., Schuster, R., Melcher, F., Meisel, T. & Zanetti, A. 2003. Geochemistry and tectonomagmatic affinity of the Yungbwa ophiolite, SW Tibet. *Lithos* **66**, 155–72.

Mohajjel, M., Fergusson, C. & Sahandi, M. 2003. Cretaceous–Tertiary convergence and continental collision, Sanandaj–Sirjan zone, western Iran. *Journal of Asian Earth Sciences* **21**, 397–412.

Morgan, Z., Liang, Y. & Kelemen, P. 2008. Significance of the concentration gradients associated with dunite bodies in the Josephine and Trinity ophiolites. *Geochemistry, Geophysics, Geosystems* **9**, Q07025. doi: 10.1029/2008GC001954.

Morimoto, N. 1988. The nomenclature of pyroxenes. *Mineralogical Magazine* **52**, 350–535.

Morishita, T., Maeda, J., Miyashita, S., Kumagai, H., Matsumoto, T. & Dick, H. J. B. 2007. Petrology of local concentration of chromian spinel in dunite from the slow-spreading South West Indian Ridge. *European Journal Mineralogy* **19**, 871–82.

Moseley, D. 1984. Symplectic exsolution in olivine. *American Mineralogist* **69**, 139–53.

Mysen, B. O. & Kushiro, I. 1977. Compositional variations of coexisting phases with degree of melting of peridotite in the upper mantle. *American Mineralogist* **62**, 843–56.

Nicolas, A. & Prinzhofer, A. 1983. Cumulative or residual origin for the transition zone in ophiolites: structural evidence. *Journal of Petrology* **24**, 188–206.

Niu, Y. 1997. Mantle melting and melt extraction processes beneath ocean ridges: evidence from abyssal peridotites. *Journal of Petrology* **38**, 1047–74.

Niu, Y. 2004. Bulk-rock major and trace element compositions of abyssal peridotites: implications for mantle melting, melt extraction and post-melting processes beneath mid ocean ridges. *Journal of Petrology* **45**, 2423–58.

Niu, Y., Langmuir, C. H. & Kinzler, R. J. 1997. The origin of abyssal peridotites: a new perspective. *Earth and Planetary Science Letters* **152**, 251–65.

Niu, Y. & O'Hara, M. J. 2003. Origin of ocean island basalts: a new perspective from petrology, geochemistry, and mineral physics considerations. *Journal of Geophysical Research* **108**, 2209. doi: 10.1029/2002JB002048.

Niu, X., Yang, J., Dilek, Y., Xu, J., Li, J., Chen, S., Feng, G., Liu, F., Xiong, F. & Liu, Z. 2015. Petrological and Os isotopic constraints on the origin of the Dongbo peridotite massif, Yarlung Zangbo Suture Zone, Western Tibet. *Journal of Asian Earth Sciences* **110**, 72–84.

Nouri, F. 2016. *Geochemistry and geodynamics of intrusive and volcanic bodies in Harsin area (West of Iran)*. Ph.D. thesis, Tarbait Modares University, Tehran, Iran. Published thesis.

Nouri, F., Asahara, Y., Azizi, H., Yamamoto, K. & Tsuboi, M. 2017. Geochemistry and petrogensis of the Eocene back arc mafic rocks in the Zagros suture zone, northern Noorabad, western Iran. *Chemie der Erde / Geochemistry* **22**, 517–33.

Nouri, F. & Azizi, H. 2015. The rodingitization of gabbroic bodies in the southeast of Sahneh (west of Iran) with emphasis on mineral reaction and isotope geochemistry. *Iranian Journal of Science Kharazmi University* **16**, 107—24 (in Persian).

Nouri, F., Azizi, H., Golonka, J., Asahara, Y., Orihashi, Y., Yamamoto, K., Tsuboi, M. & Anma, R. 2016. Age and petrogenesis of Na-rich felsic rocks in western Iran: evidence for closure of the southern branch of the Neo-Tethys in the Late Cretaceous. *Tectonophysics* **671**, 151–72.

Omrani, J., Agard, P., Whitechurch, H., Benoit, M., Prouteau, G. & Jolivet, L. 2008. Arc-magmatism and subduction history beneath the Zagros Mountains, Iran: a new report of adakites and geodynamic consequences. *Lithos* **106**, 380–98.

Pagé, P., Bédard, J. H. & Tremblay, A. 2009. Geochemical variations in a depleted fore-arc mantle: the Ordovician Thetford Mines Ophiolite. *Lithos* **113**, 21–47.

Palme, H. & O'Neill, H. St C. 2004. Cosmochemical estimates of mantle composition. In *Treatise on Geochemistry*, 2nd edn (eds H.D. Holland & K.K. Turrekian), pp. 1–38. Amsterdam: Elsevier.

Palmer, M. R. & Edmond, J. M. 1989. The strontium isotope budget of the modern ocean. *Earth and Planetary Science Letters* **92**, 11–26.

Parkinson, I. J. & Pearce, J. A. 1998. Peridotites from the Izu–Bonin–Mariana forearc (ODP Leg 125): evidence for mantle melting and melt–mantle interaction in a supra-subduction zone setting. *Journal of Petrology* **39**, 1577–618.

Parkinson, I., Pearce, J. A., Thirlwall, M. E. A., Johnson, K. T. M. & Ingram, G. 1992. Trace element geochemistry of peridotites from the Izu-Bonin-Mariana forearc, Leg 125. *Proceedings of the Ocean Drilling Program, Scientific Results* **125**, 487–506.

Parlak, O., Höck, V. & Delaloye, M. 2002. The supra-subduction zone Pozanti–Karsanti ophiolite, southern Turkey: evidence for high-pressure crystal fractionation of ultramafic cumulates. *Lithos* **65**, 205–24.

Paulick, H., Bach, W., Godard, M., De Hoog, J. C. M., Suhr, G. & Harvey, J. 2006. Geochemistry of abyssal peridotites (Mid-Atlantic Ridge, 15°20′ N, ODP Leg 209): implications for fluid/rock interaction in slow spreading environments. *Chemical Geology* **234**, 179–210.

Pearce, J. A., Barker, P. F., Edwards, S. J., Parkinson, I. J. & Leat, P. T. 2000. Geochemistry and tectonic significance of peridotites from the South Sandwich arc–basin system, South Atlantic. *Contributions to Mineralogy and Petrology* **139**, 36–53.

Pearce, J. A. & Robinson, P. T. 2010. The Troodos ophiolitic complex probably formed in a subduction initiation, slab edge setting. *Gondwana Research* **18**, 60–81.

Piccardo, G. B., Müntener, O., Zanetti, A. & Pettke, T. 2003. Ophiolitic pridotites of the Alpine-Apennine system: mantle processes and geodynamic relevance. *International Geology Review* **40**, 1119–59.

Piepgras, D. J. & Wasserburg, G. J. 1987. Rare-earth element transport in the western North Atlantic inferred from Nd isotopic observations. *Geochimica et Cosmochimica Acta* **51**, 1257–71.

Rafia, R. & Shahidi, A. 2006. *Geological Map of Miyanrahan*. Quadrangle 5459. Tehran: Geological Survey of Iran.

Ricou, L. E. 1994. Tethys reconstructed plate's continental fragments and their boundaries since 260 Ma from Central America to South-eastern Asia. *Geodinamica Acta* **7**, 169–218.

Roeder, P. L., Poustovetov, A. & Oskarsson, N. 2001. Growth forms and composition of chromian spinel in MORB magma: diffusion-controlled crystallization of chromian spinel. *Canadian Mineralogist* **39**, 397–416.

Saccani, E., Allahyari, K., Beccaluva, L. & Bianchini, G. 2013. Geochemistry and petrology of the Kermanshah ophiolites (Iran): implication for the interaction between passive rifting, oceanic accretion, and OIB-type components in the Southern Neo-Tethys Ocean. *Gondwana Research* **24**, 392–411.

Sadeghian, M. & Delvar, S. T. 2006. *Geological Map of Kamyaran*. Quadrangle 5359. Tehran: Geological Survey of Iran.

Saka, S., Uysal, I., Akmaz, R. M., Kaliwoda, M. & Hochleitner, R. 2014. The effects of partial melting, melt–mantle interaction and fractionation on ophiolite generation: constraints from the late Cretaceous Pozantı-Karsantı ophiolite, southern Turkey. *Lithos* **202**, 300–16.

Salters, V. J. M. & Stracke, A. 2004. Composition of the depleted mantle. *Geochemistry, Geophysics, Geosystems* **5**, Q05004. doi: 10.1029/2003GC000597.

Savov, I. P., Ryan, J. G., D'Antonio, M. & Fryer, P. 2007. Shallow slab fluid release across and along the Mariana arc-basin system: insights from geochemistry of serpentinized peridotites from the Mariana fore arc. *Journal of Geophysical Research* **112**, B09205. doi: 10.1029/2006JB004749.

Savov, I. P., Ryan, J. G., D'Antonio, M., Kelley, K. & Mattie, P. 2005. Geochemistry of serpentinized peridotites from the Mariana fore arc conical seamount, ODP Leg 125: implications for the elemental recycling at subduction zones. *Geochemistry, Geophysics, Geosystems* **6**, Q04J15. doi: 10.1029/2004GC000777.

Seifert, K. & Brunotte, D. 1996. Geochemistry of serpentinized mantle peridotite from site 897 in the Iberia Abyssal Plain. *Proceedings of the Ocean Drilling Program, Scientific Results* **149**, 413–24.

Seyler, M. & Bonatti, E. 1997. Regional scale melt–rock interaction in lherzolitic mantle in the Romanche Fracture Zone (Atlantic Ocean). *Earth and Planetary Science Letters* **146**, 273–87.

Seyler, M., Lorand, J. P., Dick, H. J. B. & Drouin, M. 2007. Pervasive melt percolation reactions in ultra-depleted refractory harzburgites at the Mid-Atlantic Ridge, 15200N: ODP Hole 1274A. *Contributions to Mineralogy and Petrology* **153**, 303–19.

Seyler, M., Toplis, M. J., Lorand, J. P., Luguet, A. & Cannat, M. 2001. Clinopyroxene microtextures reveal incompletely extracted melts in abyssal peridotites. *Geology* **29**, 155–8.

Shafaii Moghadam, H. & Stern, R. 2015. Ophiolites of Iran: keys to understanding the tectonic evolution of SW Asia: (II) Mesozoic ophiolites. *Journal of Asian Earth Sciences* **100**, 31–56.

Shafaii Moghadam, H., Stern, R. J., Chiaradia, M. & Rahgoshay, M. 2013. Geochemistry and tectonic evolution of the Late Cretaceous Gugher-Baft ophiolite, central Iran. *Lithos* **168**, 33–47.

Shafaii Moghadam, H., Zaki Khedr, M., Chiaradia, M., Stern, R. J., Bakhshizad, F., Arai, S., Ottley, C. J. & Tamura, A. 2014. Supra-subduction zone magmatism of the Neyriz ophiolite, Iran: constraints from geochemistry and Sr-Nd-Pb isotopes. *International Geology Review* **56**, 1395–412.

Shahabpour, J. 2007. Island arc affinity of the central Iranian volcanic belt. *Journal of Asian Earth Sciences* **30**, 652–65.

Shahidi, A. & Nazari, H. 1997. *Geological Map of Harsin*. Quadrangle 5558. Tehran: Geological Survey of Iran.

Siena, F. & Coltorti, M. 1993. Thermo barometric evolution and metasomatic processes of upper mantle in different tectonic settings: evidence from spinel peridotite xenoliths. *European Journal of Mineralogy* **5**, 1073–90.

Stakes, D. S. & Franklin, J. M. 1994. Petrology of igneous rocks at Middle Valley, Juan de Fuca Ridge. *In Proceedings of the Ocean Drilling Program, Scientific Results* **139**, 79–102.

Stöcklin, J. 1968. Structural history and tectonics of Iran: a review. *American Association of Petroleum Geologists* **52**, 1229–58.

Stracke, A., Bizimis, M. & Salters, V. J. 2003. Recycling oceanic crust: quantitative constraints. *Geochemistry, Geophysics, Geosystems* **4**, 8003. doi: 10.1029/2001GC000223.

Su, Y. & Langmuir, C. H. 2003. *Global MORB chemistry compilation at the segment scale*. Ph.D. thesis, Columbia University, New York. Published thesis.

Suhr, G. 1999. Melt migration under oceanic ridges: inferences from reactive transport modelling of upper mantle hosted dunites. *Journal of Petrology* **40**, 575–99.

Suhr, G., Hellebrand, E., Snow, J. E., Seck, H. A. & Hofmann, A. W. 2003. Significance of large, refractory dunite bodies in the upper mantle of the Bay of Islands Ophiolite. *Geochemistry, Geophysics, Geosystems* **4**, 8605.

Sun, S. S. & McDonough, W. F. 1989. Chemical and isotopic systematic of oceanic basalts: implication for mantle composition and processes. In *Magmatism in the Oceanic Basins* (eds A. D. Sunders & M. J. Norry), pp. 313–45. Geological Society of London, Special Publication no. 42.

Tachikawa, K., Jeandel, C. & Roy Barman, M. 1999. A new approach to the Nd residence time in the ocean: the role of atmospheric inputs. *Earth and Planetary Science Letters* **170**, 433–46.

Tamura, A. & Arai, S. 2005. Unmixed spinel in chromitite from the Iwanai-dake peridotite complex, Hokkaido, Japan: a reaction between peridotite and highly oxidized magma in the mantle wedge. *American Mineralogist* **90**, 473–80.

Tamura, A., Arai, A., Ishimaru, S. & Andal, E. S. 2008. Petrology and geochemistry of peridotites from IODP Site U1309 at Atlantis Massif, MAR 30_N: micro and macroscale melt penetrations into peridotites. *Contributions to Mineralogy and Petrology* **155**, 491–509.

Tanaka, T., Togashi, S., Kamioka, H., Amakawa, H., Kagami, H., Hamamoto, T., Yuhara, M. *et al.* 2000. JNdi-1: a neodymium isotopic reference in consistency with LaJolla neodymium. *Chemical Geology* **168**, 279–81.

Turekian, K. K. 1968. *Oceans*. Englewood Cliffs, New Jersey: Prentice-Hall, 120 pp.

Ulrich, M., Picard, C., Guillot, S., Chauvel, C., Cluzel, D. & Meffre, S. 2010. Multiple melting stages and refertilization as indicators for ridge to subduction formation: the New Caledonia ophiolite. *Lithos* **115**, 223–36.

Uysal, I., Ersoy, E. Y., Dilek, Y., Escayola, M., Sarifakioğlu, E., Saka, S. & Hirata, T. 2015. Depletion and refertilization of the Tethyan oceanic upper mantle as revealed by the early Jurassic Refahiye ophiolite, NE Anatolia – Turkey. *Gondwana Research* **27**, 594–611.

Uysal, I., Ersoy, E. Y., Dilek, Y., Kapsiotis, A. & Sarifakioğlu, E. 2016. Multiple episodes of partial melting, depletion, metasomatism and enrichment processes recorded in the heterogeneous upper mantle sequence of the Neotethyan Eldivan ophiolite, Turkey. *Lithos* **246**, 228–45.

Uysal, İ., Ersoy, E. Y., Karsli, O., Dilek, Y., Sadiklar, M. B., Ottley, C. J., Tiepolo, M. & Meisel, T. 2012. Coexistence of abyssal and ultra-depleted SSZ type mantle peridotites in a Neo Tethyan Ophiolite in SW Turkey: constraints from mineral composition, whole-rock geochemistry (major–trace–REE–PGE), and Re–Os isotope systematics. *Lithos* **132**, 50–69.

Van der Laan, S. R., Arculus, R. J., Pearce, J. A. & Murton, B. J. 1992. Petrography, mineral chemistry, and phase relations of the basement boninite series of site 786, Izu-Bonin forearc. *Proceedings of the Ocean Drilling Program, Scientific Results* **125**, 171–201.

Verdel, C., Wernicke, B. P., Hassanzadeh, J. & Guest, B. 2011. A Paleogene extensional arc flare up in Iran. *Tectonics* **30**, 1–20.

Whattam, S. A., Cho, M. & Smith, I. E. 2011. Magmatic peridotites and pyroxenites, Andong Ultramafic Complex, Korea: geochemical evidence for supra-subduction zone formation and extensive melt–rock interaction. *Lithos* **127**, 599–618.

White, W. M. & Hofmann, A.W. 1982. Sr and Nd isotope geochemistry of oceanic basalts and mantle evolution. *Nature* **296**, 821–25.

Whitechurch, H., Omrani, J., Agard, P., Humbert, F., Montigny, R. & Jolivet, L. 2013. Evidence for Paleocene–Eocene evolution of the foot of the Eurasian margin (Kermanshah ophiolite, SW Iran) from back-arc to arc: implications for regional geodynamics and obduction. *Lithos* **182–183**, 11–32.

Whitney, D. L. & Evans, B. W. 2010. Abbreviations for names of rock forming minerals. *American Mineralogist* **95**, 185–7.

Workman, R. K. & Hart, S. R. 2005. Major and trace element composition of the depleted MORB mantle (DMM). *Earth and Planetary Science Letters* **231**, 53–72.

Wrobel Daveau, J. C., Ringenbach, J. C., Tavakoli, S., Ruiz, G., Masse, P. & Frizonde Lamotte, D. 2010. Evidence for mantle exhumation along the Arabian margin in the Zagros (Kermanshah area, Iran). *Arabian Journal of Geosciences* **3**, 499–513.

Xu, Y., Ma, J. L., Huang, X. L., Lizuka, Y., Chung, S., Wang, Y. B. & Wu, X. 2004. Early Cretaceous gabbroic complex from Yinan, Shandong Province, petrogenesis and mantle domains beneath the North China Craton. *International Journal of Earth Sciences* **93**, 1025–41.

Zhou, M. & Kerrich, R. 1992. Morphology and composition of chromite in komatiites from the Belingwe Greenstone Belt, Zimbabwe. *Canadian Mineralogist* **30**, 303–17.

Zhou, M. F., Robinson, P. T., Malpas, J., Edwards, S. J. & Qi, L. 2005. REE and PGE geochemical constraints on the formation of dunites in the Luobusa ophiolite, Southern Tibet. *Journal of Petrology* **46**, 615–39.